

Bayesian Windkessel calibration using optimized 0D surrogate models

Jakob Richter,^{1,2} Jonas Nitzler,^{2,3} Luca Pegolotti,^{1,4} Karthik Menon,^{1,4} Jonas Biehler,² Wolfgang A. Wall,² Daniele E. Schiavazzi,⁵ Alison L. Marsden,^{1,4} Martin R. Pfaller^{1,4}

Affiliations

1. Department of Pediatrics, Stanford University
2. Institute for Computational Mechanics, Technical University of Munich
3. Professorship for Data-driven Materials Modeling, Technical University of Munich
4. Institute for Computational and Mathematical Engineering, Stanford University
5. Department of Applied and Computational Mathematics and Statistics, University of Notre Dame

Abstract

Bayesian boundary condition (BC) calibration approaches from clinical measurements have successfully quantified inherent uncertainties in cardiovascular fluid dynamics simulations. However, estimating the posterior distribution for all BC parameters in three-dimensional (3D) simulations has been unattainable due to infeasible computational demand. We propose an efficient method to identify Windkessel parameter posteriors: We only evaluate the 3D model once for an initial choice of BCs and use the result to create a highly accurate zero-dimensional (0D) surrogate. We then perform Sequential Monte Carlo (SMC) using the optimized 0D model to derive the high-dimensional Windkessel BC posterior distribution. Optimizing 0D models to match 3D data a priori lowered their median approximation error by nearly one order of magnitude in 72 publicly available vascular models. The optimized 0D models generalized well to a wide range of BCs. Using SMC, we evaluated the high-dimensional Windkessel parameter posterior for different measured signal-to-noise ratios in a vascular model, which we validated against a 3D posterior. The minimal computational demand of our method using a single 3D simulation, combined with the open-source nature of all software and data used in this work, will increase access and efficiency of Bayesian Windkessel calibration in cardiovascular fluid dynamics simulations.

1 Introduction

Subject-specific Computational Fluid Dynamics (CFD) is an emerging tool in the treatment of cardiovascular diseases [1]. Such CFD models require solving an initial boundary value problem where the domain of interest is commonly modeled with high-fidelity three-dimensional (3D) models while zero-dimensional (0D) boundary conditions (BCs) physiologically approximate the downstream vasculature (Figure 1, left). A common choice for BCs is the three-element Windkessel model [2], which approximates the vascular resistance and compliance of distal vascular beds that are not resolved in image data and computationally intractable in 3D simulations. 0D models (Figure 1, middle and right) can estimate bulk blood flow and pressure at a fraction of the computational cost [3] of 3D simulations. In addition, 0D models are used as efficient (albeit sometimes less accurate) substitutes for 3D models in the simulation domain, e.g., to predict the pressure drop in aortic coarctations [4] or coronary arteries [5]. They are especially useful in combination with 3D models in many-query settings, such as uncertainty quantification or optimization problems involving thousands of model evaluations [6].

Windkessel BC parameters are patient-specific, meaning they must be calibrated for each patient based on clinical measurements [7], typically from 4D flow magnetic resonance imaging (MRI) or Doppler ultrasound flow measurements and catheter or cuff pressure measurements. In the following,

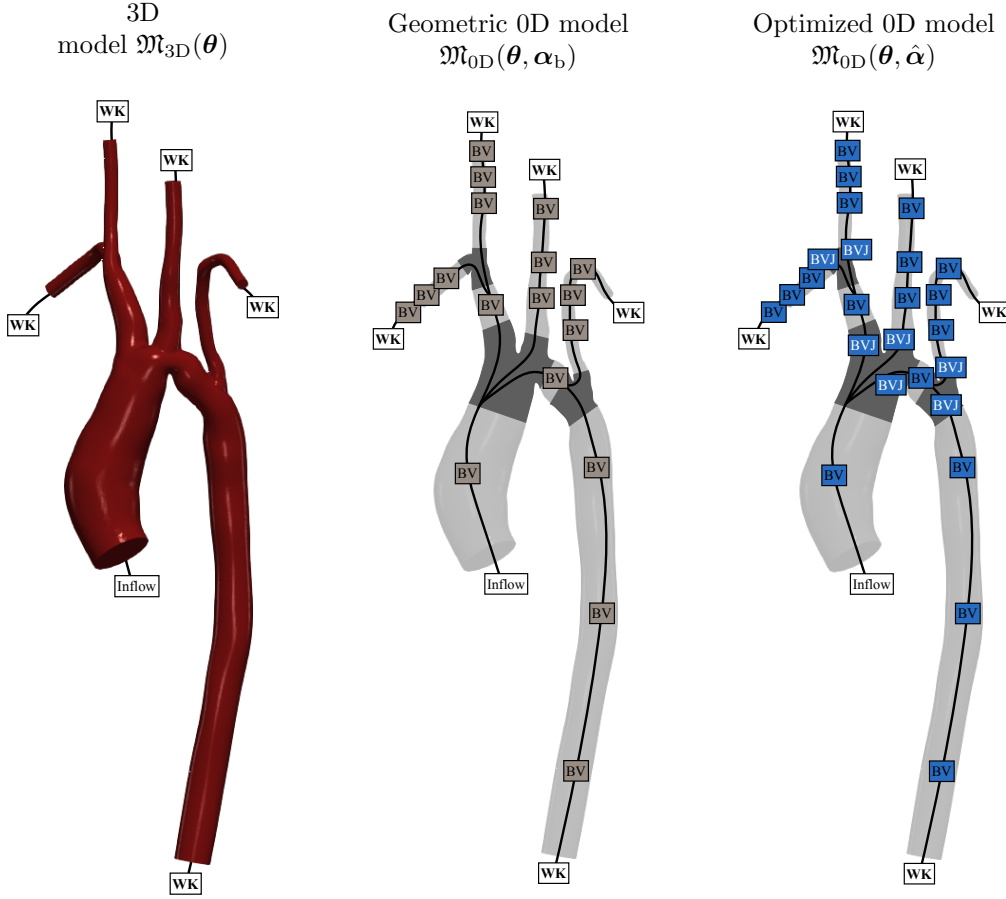


Figure 1: Illustration of different blood flow models used in this work. Inflow (Inflow) and Windkessel boundary conditions (WK) with parameters θ are identical in all models. The geometry model is separated into branch (light) and junction (dark) regions. The *geometric* 0D model (middle) consists of **BloodVessel** elements (BV) for branches with parameters α_b derived purely from the 3D geometry. The *optimized* 0D model (right) includes additional **BloodVesselJunction** elements (BVJ) for junctions and all parameters $\hat{\alpha}$ are optimized from 3D simulation results.

these clinical measurements are referred to as observations. These observations are usually corrupted by noise, for example, from the limited accuracy of a measurement device or the unpredictable positioning of a sensor. BCs estimated based on these measurements are thus more accurately represented by a probability distribution over a range of possible values rather than discrete parameter values. The benefit of quantifying these inherent uncertainties is twofold. First, it provides a measure of confidence when selecting a discrete point estimate of BCs for further analysis. Second, we can further propagate the uncertainties in BCs to uncertainties in model predictions for clinical decision-making. In this work, we infer the posterior distribution of BC parameters given noisy clinical observations. Our algorithm requires only minimal 3D simulation costs, i.e., only a single fully resolved 3D simulation over one cardiac cycle. To achieve this, we propose two novel techniques. First, we present a fast deterministic optimization method to yield a highly accurate 0D model from 3D data. Second, we use the 0D model to predict the sought posterior distribution of the BC parameters given noisy observations.

The accuracy of 0D models compared to 3D fluid dynamics has been extensively quantified in previous studies [5, 8, 9, 10, 3]. Automatic or semi-automatic tools generate these 0D models from 3D geometries, which typically achieve maximum approximation errors of bulk flow and pressure at their outlets of around 10%, depending on the anatomy and the error metric used. In some examples, resistances in 0D models have been calibrated semi-automatically or automatically to improve agreement between 0D and 3D simulations. For pulmonary models, Lan et al. [11] used a derivative-free Nelder-Mead optimization, whereas Lee et al. [12] used iterative linear corrections. Tran et al. [13] iteratively refined scaling global factors for key coronary model outputs. In this work, we propose a deterministic least-squares procedure to optimize a 0D model to match an initial 3D model. Our algorithm optimizes all 0D parameters in the model, i.e., resistances, inductances, capacitances, and non-linear stenosis factors. Our 0D optimization method approximates the given data in a least-squares sense, which makes it applicable to arbitrary vascular anatomies. In this work, we demonstrate its use in aorta, aortafemoral, coronary, and pulmonary models.

We refer to Marsden [14] for a general overview of optimization in cardiovascular modeling and to Ninos et al. [15] for an overview of uncertainty quantification (UQ) in hemodynamics. Furthermore, we point out efficient developments in multi-fidelity uncertainty quantification [16, 17, 18, 19], which are especially useful for large-scale coupled problems, and can drastically accelerate the otherwise expensive calculations. Different strategies have been demonstrated to calibrate the parameters of Windkessel BCs [20]. Spilker et al. [21] estimated Windkessel parameters by solving a system of non-linear equations using a quasi-Newton method informed by a 0D surrogate to compute the initial Jacobian. Ismail et al. [22] proposed an adjoint-based approach to compute the initial Jacobian, thereby reducing the sensitivity to accurate initial guesses. Tran et al. [13] and Menon et al. [23, 24] used derivative-free optimization to estimate high-dimensional Windkessel as well as other 0D BC parameters for coronary hemodynamics models informed by clinical measurements of cardiac function and coronary perfusion. However, deterministic optimization is prone to get stuck in unfavorable local optima, especially in the presence of experimental noise [20]. More robust approaches are based on *Bayesian* calibration, which interprets the calibration as a statistical inference task, treating all variables as distributions. Here, the solution is captured by a probability distribution for the parameters. Pant et al. [25] demonstrated the application of Kalman filters for Windkessel calibration using an unscented Kalman filter (UKF). The UKF was applied to a 0D surrogate of the 3D model, which itself was subsequently recalibrated based on 3D simulation results. Kalman filters sequentially incorporate observations about a dynamic process (like time-dependent clinical measurements) by propagating the mean and variance of the current parameter estimate and correcting the latter based on the observations. The UKF is a special form of Kalman filter, where dedicated control points are chosen for the forward propagation to reduce the number of required model evaluations [25]. Nevertheless, Kalman filters can only approximate Gaussian distributions. It has been shown, however, that posterior distributions in cardiovascular BCs deviate from Gaussian distributions, sometimes even exhibiting multiple modes [26]. Other methods use multi-fidelity approaches that rely on iteratively sampling the parameter space and learning a relationship between high-fidelity 3D models and low-fidelity 0D or one-dimensional (1D) models [27, 28].

In this work, we propose a new framework for calibrating Windkessel parameters in cardiovascular models using Sequential Monte Carlo (SMC). As in Kalman filter approaches, the calibration problem is stated as a Bayesian inference task, and the result is given as the full posterior distribution over BC parameters given the observations. The probabilistic approach also incorporates prior knowledge

about the BC parameters and information about the noise structure in, e.g., clinical measurements used for the calibration. SMC is employed to solve the Bayesian calibration problem. SMC can capture arbitrary posteriors, including multimodal distributions. By exploring intermediate distributions between the prior and the posterior, sampling is sequentially refined in regions with high posterior density, leading to computational savings. In our work, the workload of the Bayesian calibration is completely shifted to 0D models. The 0D models are deterministically optimized to a single 3D simulation, enabling the Bayesian calibration’s accuracy. This yields highly accurate 0D models in unprecedented agreement with the corresponding high-fidelity 3D models.

The remainder of this work is structured as follows: In Section 2, we outline the basic concepts for 3D and 0D modeling and the optimization and Bayesian calibration methods employed in this work. Section 3 presents the results of the 0D model optimization and BC calibration algorithms and validates the results against the high-fidelity 3D model. Section 4 summarizes the results of this work and provides an outlook for future work.

2 Methods

In this section, we introduce Bayesian Windkessel calibration (2.1). Further, we briefly review governing equations for high-fidelity three-dimensional (3D) (2.2) and surrogate zero-dimensional (0D) (2.3) blood flow models. We then extend these to the inverse problem of optimizing 0D models (2.4).

2.1 Bayesian Windkessel calibration with optimized 0D models

The goal of the Bayesian boundary condition (BC) calibration is to infer a posterior distribution $p_{0D}(\theta|\mathbf{y}_{\text{obs}}, \alpha)$ for the Windkessel BC parameters θ , informed by uncertain clinical observations \mathbf{y}_{obs} . We perform this using a 0D model \mathfrak{M}_{0D} with internal 0D element parameters α . The distinction between the Windkessel BC parameters θ and the 0D element parameters α is crucial for the following discussion and will be explained in detail below. In the following, we introduce probabilistic calibration (2.1.1), describe the likelihood model selection in this work (2.1.2), and present the Sequential Monte Carlo (SMC) algorithm (2.1.3).

2.1.1 Bayesian calibration

The posterior distribution reflects the solution of the calibration and can be derived using Bayes’ rule [29]

$$p(\theta|\mathbf{y}_{\text{obs}}) = \frac{p(\mathbf{y}_{\text{obs}}|\theta) \cdot p(\theta)}{p(\mathbf{y}_{\text{obs}})}. \quad (1)$$

The *prior distribution* $p(\theta)$ encodes the knowledge about the parameters before new data is observed. The *likelihood* $p(\mathbf{y}_{\text{obs}}|\theta)$ defines a measure of proximity between the model response $\mathbf{y} = \mathfrak{M}_{0D}(\theta)$ and the observations \mathbf{y}_{obs} . The *evidence* $p(\mathbf{y}_{\text{obs}})$ normalizes the former two components to an actual probability density. This normalization constant is typically difficult to evaluate, requiring the potentially high-dimensional integration over θ . To avoid this complexity, we take the same approach as many other algorithms by using the *unnormalized posterior*

$$p(\theta|\mathbf{y}_{\text{obs}}) \propto p(\mathbf{y}_{\text{obs}}|\theta) \cdot p(\theta), \quad (2)$$

and the logarithmic version of the latter and conduct the normalization *a posteriori*.

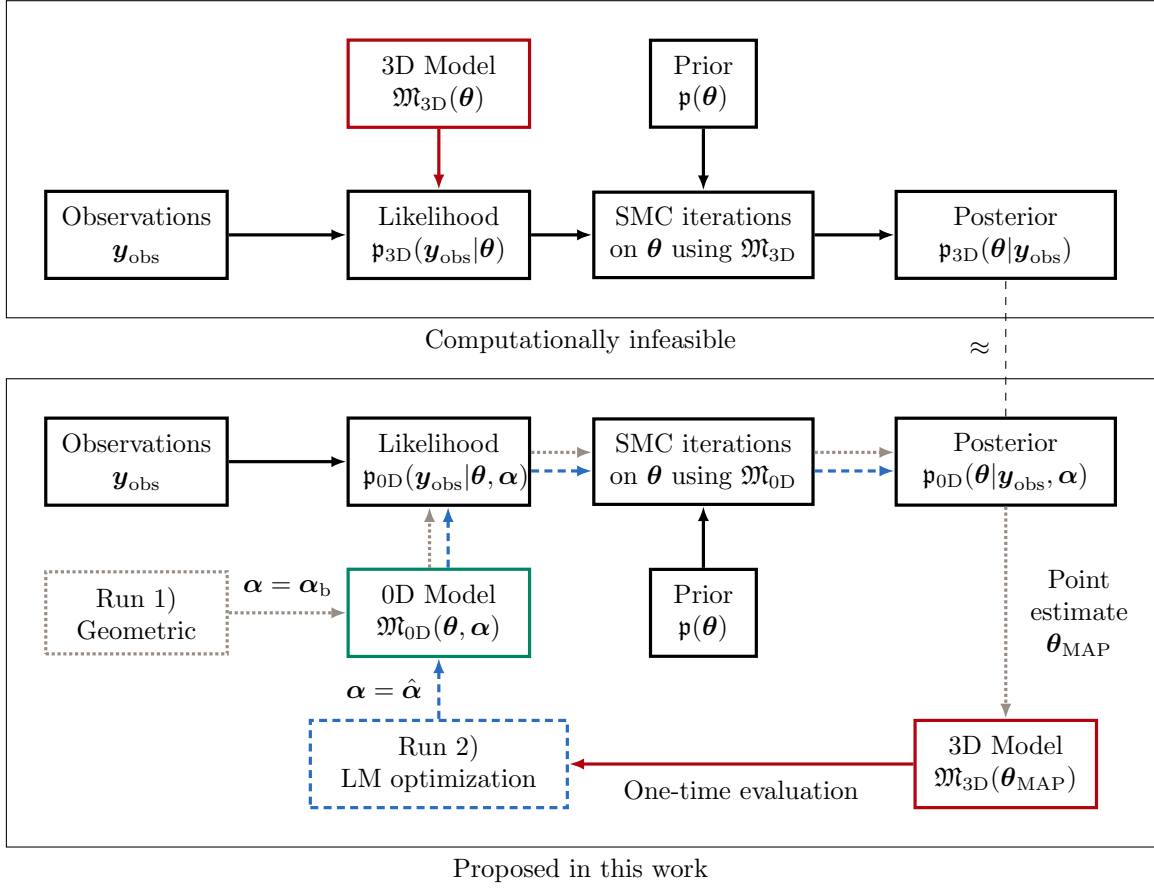


Figure 2: Framework proposed in this work for Bayesian Windkessel BC calibration, using 3D models \mathcal{M}_{3D} (expensive, red) and 0D models (cheap, green). The 0D models use geometric parameters (gray, dotted) or optimized parameters (blue, dashed).

Bayesian calibration of Windkessel BC parameters θ from observations \mathbf{y}_{obs} is a computationally challenging task. Using SMC, it easily requires thousands of model evaluations \mathcal{M} , each requiring a 3D FEM solution (Figure 1, left), to yield the posterior distribution $\mathbf{p}(\theta|\mathbf{y}_{\text{obs}})$ from a prior distribution $\mathbf{p}(\theta)$. Figure 2 (top) highlights this process using the 3D model \mathcal{M}_{3D} (red) to obtain the posterior distribution $\mathbf{p}_{3D}(\theta|\mathbf{y}_{\text{obs}})$. While this would give an exact representation of the posterior distribution, it is generally infeasible due to its excessive computational demand.

In this work, we combine models \mathcal{M}_{0D} and \mathcal{M}_{3D} in a novel calibration method visualized in Figure 2 (bottom). Here, expensive statistical model evaluation is performed exclusively with fast 0D models \mathcal{M}_{0D} (green), relying on two crucial assumptions. First, we assume that we can construct highly accurate 0D surrogate models that approximate $\mathcal{M}_{3D} \approx \mathcal{M}_{0D}$. Second, we assume that the 0D-derived posterior approximates $\mathbf{p}_{3D} \approx \mathbf{p}_{0D}$. While 0D models are orders of magnitude faster to evaluate, they are, in general, not sufficiently accurate to justify these assumptions. As part of our calibration process, we thus optimize the 0D element parameters α from a single 3D simulation to greatly enhance 0D accuracy. This also allows us to demonstrate the validity of the above two assumptions.

We perform two SMC calibration runs in the proposed calibration workflow. The first SMC run (gray) is performed using a *geometric* 0D model (Figure 1, middle) $\mathcal{M}_{0D}(\theta, \alpha_b)$ composed of **BloodVessel** elements with parameters α_b derived purely from the blood vessel’s geometry, containing the vessel branches’ resistances, inductances, capacitances, and non-linear stenosis factors (Section 2.3) [3]. This yields a first estimate for the posterior distribution $\mathbf{p}_{0D}(\theta|\mathbf{y}_{\text{obs}}, \alpha_b)$. Using the parameter set θ_{MAP} with the highest posterior density, the so-called maximum a posteriori (MAP) estimate, we perform one evaluation of the 3D model $\mathcal{M}_{3D}(\theta_{\text{MAP}})$ (Section 2.2). These results are then used to determine the *optimized* 0D model (Figure 1, right) parameters $\hat{\alpha}$, including **BloodVesselJunction** elements, using the Levenberg-Marquardt (LM) algorithm (Section 2.4). This optimization yields a

highly accurate 0D model to approximate $\mathfrak{M}_{3D}(\boldsymbol{\theta}_{\text{MAP}}) \approx \mathfrak{M}_{0D}(\boldsymbol{\theta}_{\text{MAP}}, \hat{\boldsymbol{\alpha}})$. Finally, we perform a second SMC (blue) run with the optimized 0D model $\mathfrak{M}_{0D}(\boldsymbol{\theta}, \hat{\boldsymbol{\alpha}})$ to derive the final posterior distribution $\mathfrak{p}_{0D}(\mathbf{y}_{\text{obs}}|\boldsymbol{\theta}, \hat{\boldsymbol{\alpha}})$ for the Windkessel BC parameters $\boldsymbol{\theta}$. Note that the second SMC run is independent from the first one to not introduce any bias from the geometric 0D model. Throughout this manuscript, we refer to obtaining the optimal point estimate 0D parameters $\hat{\boldsymbol{\alpha}}$ using LM as *optimization*. This is in contrast to the Bayesian *calibration* of Windkessel parameters $\boldsymbol{\theta}$ with posterior distribution $\mathfrak{p}(\boldsymbol{\theta}|\mathbf{y}_{\text{obs}})$ under uncertain observations \mathbf{y}_{obs} using SMC.

2.1.2 Zero-dimensional likelihood model

The forward model can only be evaluated pointwise, i.e., for a given set of parameters $\boldsymbol{\theta}$. The likelihood model scores the model output vector $\mathbf{y} = \mathfrak{M}_{0D}(\boldsymbol{\theta})$ for a given parameter vector $\boldsymbol{\theta}$ based on the output's proximity to the observations \mathbf{y}_{obs} . Moreover, it incorporates knowledge about the noise in the observations resulting from the clinical measurements [30]. In this work, an *additive noise* model for the observations is chosen according to Kaipio et al. [30] as

$$\mathbf{y}_{\text{obs}} = \mathbf{y} + \boldsymbol{\varepsilon} = \mathfrak{M}_{0D}(\boldsymbol{\theta}) + \boldsymbol{\varepsilon}. \quad (3)$$

For simplicity, the noise is assumed to be normally distributed with zero mean and covariance matrix $\boldsymbol{\Sigma}$, i.e., $\boldsymbol{\varepsilon} \sim \mathcal{N}(\mathbf{0}, \boldsymbol{\Sigma})$. The covariance matrix is further assumed to be diagonal wherein the variance vector $\boldsymbol{\sigma}^2$ denotes the diagonal entries of $\boldsymbol{\Sigma}$. We choose the commonly used Gaussian likelihood model here, which is defined as:

$$\mathfrak{p}(\mathbf{y}_{\text{obs}}|\boldsymbol{\theta}) = \frac{1}{\sqrt{(2\pi)^n \det \boldsymbol{\Sigma}}} \exp \left[-\frac{1}{2} (\mathfrak{M}_{0D}(\boldsymbol{\theta}) - \mathbf{y}_{\text{obs}})^\top \boldsymbol{\Sigma}^{-1} (\mathfrak{M}_{0D}(\boldsymbol{\theta}) - \mathbf{y}_{\text{obs}}) \right] \quad (4)$$

It should be noted that $\mathfrak{p}(\mathbf{y}_{\text{obs}}|\mathfrak{M}_{0D}(\boldsymbol{\theta}))$ is not a valid probability density in $\boldsymbol{\theta}$. Therefore, it is often referred to as *likelihood function* in $\boldsymbol{\theta}$. The Gaussian likelihood maximizes information entropy and thus introduces the least bias in the absence of more detailed noise information. Nevertheless, our proposed framework works with any likelihood model and can incorporate specific measurement biases from clinical measurements, introducing additional noise parameters. For example, magnetic resonance magnitude images have been shown to exhibit a Rice noise distribution [31].

2.1.3 Sequential Monte Carlo

Different methods have been developed to solve the Bayesian calibration problem. We employ the SMC algorithm, also known as particle filters [32, 33], which is described in more detail in Appendix C. The posterior distribution π in SMC is approximated by weighted particles according to

$$\mathfrak{p}(\boldsymbol{\theta}|\mathbf{y}_{\text{obs}}) \approx \sum_{i=1}^k W_{n+1}^{(i)} \delta_{\boldsymbol{\theta}_{n+1}^{(i)}}(\boldsymbol{\theta}), \quad (5)$$

with normalized weights W , number of particles k , and final iteration number n . Each particle $\delta_{\boldsymbol{\theta}_n^{(i)}}$ refers to a Dirac delta distribution at particle location $\boldsymbol{\theta}_i$. Using the parameter vector $\boldsymbol{\theta}$ with the highest posterior probability [30], the so-called MAP estimate can be computed as

$$\boldsymbol{\theta}_{\text{MAP}} = \arg \max_{\boldsymbol{\theta}} [\mathfrak{p}(\boldsymbol{\theta}|\mathbf{y}_{\text{obs}})]. \quad (6)$$

In SMC, this is equivalent to selecting the particle location $\boldsymbol{\theta}_i$ of the particle with the highest weight.

2.2 Three-dimensional blood flow modeling

The 3D model \mathfrak{M}_{3D} models blood as a Newtonian fluid in the rigid fluid domain Ω^{3D} over time T (typically several cardiac cycles) governed by the incompressible Navier-Stokes equations,

$$\nabla \cdot \boldsymbol{\sigma}(\mathbf{u}, p) = \rho [\ddot{\mathbf{u}} + (\mathbf{u} \cdot \nabla) \mathbf{u}], \quad \mathbf{x} \in \Omega^{3D}, \quad t \in [0, T], \quad (7)$$

$$\nabla \cdot \mathbf{u} = 0, \quad \mathbf{x} \in \Omega^{3D}, \quad t \in [0, T], \quad (8)$$

with velocity \mathbf{u} , pressure p , Cauchy stress tensor $\boldsymbol{\sigma} = \mu(\nabla \mathbf{u} + \nabla \mathbf{u}^T) - p\mathbf{I}$, constant density ρ , and constant dynamic viscosity μ . Throughout this manuscript, $\dot{\cdot}$ denotes a time derivative. We prescribe BCs

$$\mathbf{u}(\mathbf{x}, t) = \mathbf{0}, \quad \mathbf{x} \in \Gamma_{\text{wall}}, \quad t \in [0, T], \quad (9)$$

$$\mathbf{u}(\mathbf{x}, t) = \mathbf{u}_{\text{in}}(\mathbf{x}, t), \quad \mathbf{x} \in \Gamma_{\text{in}}, \quad t \in [0, T], \quad (10)$$

$$\mathbf{f}_{\text{WK3}}(P_i(t), Q_i(t), \boldsymbol{\theta}_i) = \mathbf{0}, \quad \mathbf{x} \in \Gamma_{\text{out},i}, \quad t \in [0, T], \quad (11)$$

$$\text{with } p(\mathbf{x}, t) = P_i(t), \quad (12)$$

$$Q_i(t) = \int_{\Gamma_{\text{out},i}} \mathbf{u}(\mathbf{x}, t) \cdot \mathbf{n} \, d\mathbf{x}, \quad (13)$$

with a no-slip BC at the vessel wall Γ_{wall} , time-dependent parabolic inflow profile \mathbf{u}_{in} at the inlet Γ_{in} . At each outlet $\Gamma_{\text{out},i}$, we prescribe a three-element Windessel BC with parameters $\boldsymbol{\theta}_i$ that relate flow rate Q_i and the pressure P_i at outlet i through an ordinary differential equation \mathbf{f}_{WK3} . Throughout this work, we use the three-element Windkessel model defined in Appendix B.5 for all outlets. We note that this choice does not restrict the BC calibration approach proposed in this work as it applies generally to any BC type. For details on the 0D-3D coupling approach, we refer to Vignon-Clementel et al. [34, 35, 36]. The initial conditions are

$$\mathbf{u}(\mathbf{x}, t = 0) = \mathbf{u}_0(\mathbf{x}), \quad \mathbf{x} \in \mathbb{R}^{3D} \quad (14)$$

$$p(\mathbf{x}, t = 0) = p_0(\mathbf{x}), \quad \mathbf{x} \in \mathbb{R}^{3D} \quad (15)$$

with initial velocity field \mathbf{u}_0 and initial pressure field p_0 , which we estimate by projecting a periodic 0D solution to the 3D geometry [37].

2.3 Zero-dimensional blood flow modeling

Analogous to electrical circuits, the elemental building blocks for blood vessels of the 0D model \mathfrak{M}_{0D} are defined as

$$\Delta P = \mathcal{R}Q, \quad \Delta P = \mathcal{L}\dot{Q}, \quad Q = \mathcal{C}\dot{P}, \quad \Delta P = \mathcal{S}Q|Q|, \quad (16)$$

with 0D parameters resistance \mathcal{R} , inductance \mathcal{L} , capacitance \mathcal{C} , and stenosis coefficient \mathcal{S} . Note that only the stenosis term depends non-linearly on the flow Q . The operator, $\Delta \bullet$ characterizes the difference between element inlet \bullet_{in} and outlet \bullet_{out} .

We use the methods outlined in Pfaffler et al. [3] to split the vessel into branches and junctions and determine values for $\mathcal{R}\mathcal{L}\mathcal{C}\mathcal{S}$ elements (16), which we combine into a **BloodVessel** lumped-parameter network (LPN) element as described in Appendix B.3. In short, we predict the branch parameter values $\boldsymbol{\alpha}_b$ of each **BloodVessel** element as

$$\mathcal{R} = \frac{8\mu l}{\pi r^4}, \quad \mathcal{L} = \frac{\rho l}{\pi r^2}, \quad \mathcal{C} = \frac{3l\pi r^3}{2Eh}, \quad \mathcal{S} = K_t \frac{\rho}{2S_0^2} \left(\frac{S_0}{S_s} - 1 \right)^2, \quad (17)$$

with dynamic viscosity μ and density ρ of blood, lumen radius r , blood vessel length l , and vessel wall Young's modulus E and thickness h . The stenosis factor \mathcal{S} includes the stenosed area S_s , proximal cross-sectional area S_0 , and empirical correction factor $K_t = 1.52$ [38]. The areas S_s and S_0 and the choice to split the branch into three segments are based on the relative extrema of the branch's cross-sectional area.

In the following sections, these models are referred to as *geometric* 0D models. We also define a **BloodVesselJunction** LPN element to connect an inlet to two or more outlets using the $\mathcal{R}\mathcal{L}\mathcal{S}$ elements with parameters $\boldsymbol{\alpha}_j$, as described in Appendix B.4. The **BloodVesselJunction** LPN element does not include a capacitance, which facilitates the derivation of the Jacobian for the zero-dimensional model optimization. Note that we do not currently infer **BloodVesselJunction** element parameters from the blood vessel geometry. Predicting junction parameters from the vessel geometry remains an active research topic [39, 40]. Thus, all junction parameters $\boldsymbol{\alpha}_j$ are set to zero in *geometric* 0D models, i.e., $\boldsymbol{\alpha}_j = \mathbf{0}$. Nevertheless, we optimize parameters for both **BloodVessel** and **BloodVesselJunction** elements in Section 2.4 using 3D simulation results. These models are referred to as *optimized* 0D models.

Connecting all elements e within a vascular tree forms a LPN with parameters $\boldsymbol{\alpha} = \boldsymbol{\alpha}_b \cup \boldsymbol{\alpha}_j$. As in the 3D model (Section 2.2), we prescribe the flow rate Q at the inlet and couple the outlets to Windkessel BCs. We assemble all elements e and BCs in our LPN into a global residual vector \mathbf{r} . The global system of differential-algebraic equations can be split by the dependence on the solution vector \mathbf{y} , containing pressures and flow-rates at LPN node points, and its time derivative $\dot{\mathbf{y}}$ as

$$\mathbf{r}(\boldsymbol{\alpha}, \mathbf{y}, \dot{\mathbf{y}}) = \mathbf{E}(\boldsymbol{\alpha}) \cdot \dot{\mathbf{y}} + \mathbf{F}(\boldsymbol{\alpha}) \cdot \mathbf{y} + \mathbf{c}(\boldsymbol{\alpha}, \mathbf{y}, \dot{\mathbf{y}}), \quad (18)$$

with constant parameter-dependent system matrices \mathbf{E} and \mathbf{F} and system vector \mathbf{c} that depends nonlinearly on \mathbf{y} and $\dot{\mathbf{y}}$. We compute pressure and flow rate associated with a given set of 0D parameters $\boldsymbol{\alpha}$ by solving

$$\text{Solve } \mathbf{r}(\boldsymbol{\alpha}, \mathbf{y}, \dot{\mathbf{y}}) \stackrel{!}{=} \mathbf{0} \text{ for } \mathbf{y}, \dot{\mathbf{y}} \text{ with given } \boldsymbol{\alpha}, \quad \text{in } \Omega^{0D}, \quad t \in [0, T], \quad (19)$$

which, in the following, is referred to as the *forward* 0D problem. The node points of the LPN, i.e., where 0D elements connect, make up the domain Ω^{0D} . We generate maps $\Omega^{0D} \rightarrow \Omega^{3D}$ and $\Omega^{3D} \rightarrow \Omega^{0D}$ through a region-growing algorithm and centerline integration, respectively, to map results between 0D and 3D models [37]. We prescribe BCs at the inlet and outlets

$$Q_j(t) = Q_{\text{in}}(t), \quad \text{on } \Gamma_{\text{in}}, \quad t \in [0, T], \quad (20)$$

$$\mathbf{f}_{\text{WK3}}(P_j(t), Q_j(t), \boldsymbol{\theta}_j) = \mathbf{0}, \quad \text{on } \Gamma_{\text{out},i}, \quad t \in [0, T], \quad (21)$$

with inflow rate Q_{in} and three-element Windkessel BCs \mathbf{f}_{WK3} corresponding to the 3D model inlet and outlet BCs $\boldsymbol{\theta}$, (10) and (11), respectively. Furthermore, we prescribe initial conditions

$$\mathbf{y}(t=0) = \bar{\mathbf{y}}, \quad (22)$$

where we obtain $\bar{\mathbf{y}}$ from a steady-state simulation with mean inflow and steady-state BCs. This lowers the number of cardiac cycles required to reach a periodic solution compared to initializing with $\mathbf{y}(t=0) = \mathbf{0}$. We use the implicit generalized- α method to discretize the forward problem (19) in time and the Newton-Raphson method to solve for the solution vector \mathbf{y} in each time step. The details of the method are given in Appendix B.1. Reusing terms from the residual (18), the Jacobian matrix \mathbf{K} for the time-discrete forward problem (19) is computed as

$$\mathbf{K} = \left. \frac{\partial \mathbf{r}}{\partial \dot{\mathbf{y}}} \right|_{\boldsymbol{\alpha}=\text{const}} = \alpha_m \left(\mathbf{E} + \frac{\partial \mathbf{c}}{\partial \dot{\mathbf{y}}} \right) + \alpha_f \gamma \Delta t_n \left(\mathbf{F} + \frac{\partial \mathbf{c}}{\partial \mathbf{y}} \right), \quad (23)$$

with time step Δt_n and time integration parameters α_f , α_m , and γ . All system matrices for the `BloodVessel`, `BloodVesselJunction`, and `Windkessel` elements can be derived analytically and are provided in Appendices B.3, B.4, and B.5, respectively.

2.4 Zero-dimensional model optimization

The proposed method for Bayesian Windkessel calibration relies on highly accurate 0D models \mathfrak{M}_{0D} that act as a surrogate for a given 3D model \mathfrak{M}_{3D} . In general, 0D models with geometric parameters $\boldsymbol{\alpha}_b$ are insufficiently accurate. In this section, we describe how to derive an optimized 0D parameter set $\hat{\boldsymbol{\alpha}}$ that better approximates $\mathfrak{M}_{3D}(\boldsymbol{\theta}_{\text{MAP}}) \approx \mathfrak{M}_{0D}(\boldsymbol{\theta}_{\text{MAP}}, \hat{\boldsymbol{\alpha}})$ for a given set of Windkessel parameters $\boldsymbol{\theta}_{\text{MAP}}$. Solving an inverse problem, we infer 0D model parameters $\hat{\boldsymbol{\alpha}}$ that optimally (in the least-squares sense) approximate given 0D solution vectors \mathbf{y} and $\dot{\mathbf{y}}$. In this work, \mathbf{y} is extracted from a 3D model \mathfrak{M}_{3D} evaluated at the parameter set $\boldsymbol{\theta}_{\text{MAP}}$. However, other sources like *in vivo* or *in vitro* measurements are also possible. The time derivative $\dot{\mathbf{y}}$ can be either taken from \mathfrak{M}_{3D} or approximated from \mathbf{y} . We use the same residual \mathbf{r} from (18) as in the forward problem (19):

$$\text{Solve } \mathbf{r}(\boldsymbol{\alpha}, \mathbf{y}, \dot{\mathbf{y}}) \stackrel{!}{=} \mathbf{0} \text{ for } \boldsymbol{\alpha} \text{ with given } \mathbf{y}, \dot{\mathbf{y}}, \quad \text{in } \Omega^{0D}. \quad (24)$$

To solve the inverse problem, we formulate (24) as a least-squares problem

$$\hat{\boldsymbol{\alpha}} = \arg \min_{\boldsymbol{\alpha}} S, \quad \text{with } S = \sum_j^D r_j^2(\boldsymbol{\alpha}, y_j, \dot{y}_j), \quad (25)$$

where $\hat{\alpha}$ is the optimal parameter set that minimizes the sum of squared residuals S , and D is the number of observations. Here, we solve for both branch and junction 0D parameters $\hat{\alpha}_b$ and $\hat{\alpha}_j$, respectively. The value D is typically given from the number of LPN node points times the number of observed time steps. Note that in case of sparse observations, the parameters $\hat{\alpha}$ might not be deterministically identifiable. We use the LM algorithm to solve the least squares problem (25) iteratively for the optimal parameter set $\hat{\alpha}$, which is described in more detail in Appendix B.2. We calculate the Jacobian for each 0D element as the gradient of the residual \mathbf{r} with respect to the 0D parameters α ,

$$\mathbf{J} = \left. \frac{\partial \mathbf{r}}{\partial \alpha} \right|_{\mathbf{y}, \dot{\mathbf{y}} = \text{const}} = \frac{\partial \mathbf{E}}{\partial \alpha} \cdot \dot{\mathbf{y}} + \frac{\partial \mathbf{F}}{\partial \alpha} \cdot \mathbf{y} + \frac{\partial \mathbf{c}}{\partial \alpha}. \quad (26)$$

Note that the solution vectors $\mathbf{y}, \dot{\mathbf{y}}$ are constant in (26), and the Jacobian can, again, be computed analytically. These terms are straightforward to derive and are given for the `BloodVessel` and `BloodVesselJunction` LPN elements in Appendices B.3 and B.4, respectively. The resulting 0D models \mathfrak{M}_{0D} with optimal parameters $\hat{\alpha} = \hat{\alpha}_b \cup \hat{\alpha}_j$ are denoted as *optimized* 0D models.

2.5 Open-source software

All results in this work were computed with open-source software. The 3D simulations were computed in SimVascular’s finite element solver `svSolver` [41]; see Esmaily Moghadam et al. [36, 42] for details. We further developed `svZeroDSolver` [43], containing the algorithmic implementation of the methods described in 2.3 and 2.4. The forward (19) and inverse problems (24) use the same residual vector \mathbf{r} (18) with linearizations with respect to the solution vector \mathbf{y} and the parameter vector α , respectively. The forward problem requires time discretization, whereas the inverse problem is simultaneously solved for all time steps. Nevertheless, the shared residual allows for reuse of large parts of the code for both problems. The system matrices for all 0D elements for forward and inverse problems are given in Appendix B. The core functionality is implemented in C++ and based on the fast linear algebra package `Eigen`. Python and C++ interfaces enable seamless integration into other software [12, 24]. The calibration framework `svSuperEstimator` [44] implements the Windkessel calibration described in Section 2.1 and interfaces different tools for performing 0D and 3D simulations, postprocessing routines and SMC Windkessel calibration. The SMC implementation is based on the Python package `particles` [45]. All 72 vascular models are publicly available from the Vascular Model Repository [46].

3 Computational results and discussion

Our results showcase the two-run process of Bayesian calibration of Windkessel boundary condition (BC) parameters θ given uncertain observations \mathbf{y}_{obs} . First, Section 3.1 demonstrates the approximation of three-dimensional (3D) models by zero-dimensional (0D) models $\mathfrak{M}_{3D}(\theta) \approx \mathfrak{M}_{0D}(\theta, \hat{\alpha})$ with optimized 0D parameters $\hat{\alpha}$. Second, Section 3.2 provides posterior distributions for BC parameters θ derived with Sequential Monte Carlo (SMC) using the optimized 0D models, $\mathfrak{p}_{3D}(\theta|\mathbf{y}_{\text{obs}}) \approx \mathfrak{p}_{0D}(\theta|\mathbf{y}_{\text{obs}}, \hat{\alpha})$.

3.1 Optimization of zero-dimensional models

In this section, we investigate the Levenberg-Marquardt (LM) 0D model optimization performance with the algorithm presented in Section 2.4. The LM optimizer derives new blood vessel and junction parameters $\hat{\alpha}$ from a 3D simulation result, enabling the approximation $\mathfrak{M}_{3D}(\theta) \approx \mathfrak{M}_{0D}(\theta, \hat{\alpha})$. The 0D models are improved in two aspects: enhancing the geometrically derived `BloodVessel` elements $\hat{\alpha}_b$, and identifying suitable parameters for `BloodVesselJunction` elements $\hat{\alpha}_j$ (which are zero in geometric 0D models). We obtain the time derivative $\dot{\mathbf{y}}$ by fitting a periodic cubic spline to \mathbf{y} , taking its derivative, and resampling the solution to 100 time points. The number of data points D was thus 100 times the number of lumped-parameter network (LPN) node points, which ranged from 28 in aortas to 1460 in pulmonary arteries (mean 274).

To demonstrate the robustness of the 0D model optimization, we demonstrate the results on a large dataset of 72 vascular models, each with given Windkessel BC parameters θ_{VMR} that were calibrated in prior studies. This openly available dataset [46] is taken from Pfaller et al. [3] and visualized

in Figure 7. It includes diverse vascular anatomies, including aortas, aortofemoral, pulmonary, and coronary arteries. Vascular states include normal, (artificial) aortic coarctation, Kawasaki disease, single ventricle disease, Marfan syndrome, abdominal aortic aneurysm, pulmonary artery hypertension, and others. Note that the 3D dataset has rigid walls, corresponding to a theoretical 0D capacitance of $\mathcal{C} = 0$. However, we found that using a small non-zero value for \mathcal{C} , thus modeling a nearly rigid wall, is beneficial for 0D numerical performance [3]. For completeness, we still report results for \mathcal{C} in this section despite it not having a physical meaning in our 0D models.

We first verify in Section 3.1.1 that we can identify 0D branch parameters $\hat{\alpha}_b$ from an optimization given ground truth 0D models with geometric branch parameters α_b . We then demonstrate in Section 3.1.2 the accuracy of 0D models $\mathfrak{M}_{0D}(\theta_{VMR}, \hat{\alpha})$ with parameters $\hat{\alpha}$ optimized from 3D models $\mathfrak{M}_{3D}(\theta_{VMR})$. Finally, we verify in Section 3.1.3 that the optimized 0D models generalize well to a wide range of BC parameters θ . These results confirm that we can confidently use optimized 0D models for the approximation $\mathfrak{M}_{3D}(\theta) \approx \mathfrak{M}_{0D}(\theta, \hat{\alpha})$ in the Bayesian Windkessel calibration in Section 3.2.

3.1.1 Identifying zero-dimensional parameters from ground truth data

As a first step in assessing the 0D element optimization proposed in Section 2.4, we verify that our optimization can successfully recover ground truth 0D geometric branch parameters α_b from \mathfrak{M}_{0D} data:

$$\text{Compare } \hat{\alpha}_b \text{ vs. } \alpha_b \text{ with } \hat{\alpha}_b = \arg \min_{\alpha} \|\mathbf{r}(\alpha, \mathfrak{M}_{0D}(\theta_{VMR}, \alpha_b))\|^2. \quad (27)$$

In the absence of any 3D-0D model discrepancy, the optimization should be able to perfectly recover the ground truth 0D parameters $\hat{\alpha}_b \approx \alpha_b$. Recall from Section 1 that $\alpha_j = \mathbf{0}$ in all geometric models which results in optimized junction parameters $\hat{\alpha}_j = \mathbf{0}$. We ran forward models \mathfrak{M}_{0D} for all 72 geometric models with Windkessel BCs θ_{VMR} from the Vascular Model Repository to generate the ground truth data. We extracted the solution of pressures and flow rates and their time derivatives from each model at all node points of the 0D LPNs. We initialized all 0D parameters $\alpha = \mathbf{0}$ to not introduce any bias to the optimized parameters $\hat{\alpha}$. Providing $\mathfrak{M}_{0D}(\theta_{VMR}, \alpha_b)$ as input, we performed LM optimization and obtained results for the optimized branch parameters $\hat{\alpha}_b$.

Due to the efficient C++ implementation and fast Python interface of `svZeroDSolver`, running all 72 forward 0D simulations and optimizations took only 47 s and 101 s on a single core, respectively. The optimization typically converged in less than ten iterations, although three coronary models stagnated at residual norms slightly above the tolerances defined in Appendix B.2. This could be due to pressures and flow rates spanning different orders of magnitude in the aorta and coronary arteries, which could be prevented by normalization. We provide a detailed overview of all optimized parameters $\hat{\alpha}_b$ vs. ground truth geometric parameters α_b in Figure 12 in Appendix D, showing \mathcal{R} , \mathcal{L} , \mathcal{C} , and \mathcal{S} for every branch. The mean of the coefficients of determination averaged over all 72 models and their branches was $R_{\mathcal{R}}^2 = R_{\mathcal{L}}^2 = R_{\mathcal{C}}^2 = 1.0$. For the stenosis coefficient, this value was slightly reduced to $R_{\mathcal{S}}^2 = 0.95$.

These results confirm that the four parameters of the `BloodVessel` element, \mathcal{R} , \mathcal{L} , \mathcal{C} , and \mathcal{S} are identifiable from the solution vector \mathbf{y} and its time derivative $\dot{\mathbf{y}}$. The slightly lower value $R_{\mathcal{S}}^2$ of the stenosis coefficient indicates that it is more difficult to identify. However, it should be noted that many of the stenosis parameters \mathcal{S} in the geometric 0D models are negligibly small and have little influence on the result, which makes them difficult to identify. The stenosis parameter is well identifiable in models with pathological stenoses, like in aortic coarctations.

3.1.2 Optimizing zero-dimensional models to three-dimensional data

We demonstrated in 3.1.1 the excellent identifiability of 0D parameters from ground truth data using the LM optimization. In this section, we quantify how well optimized 0D models \mathfrak{M}_{0D} approximate high-fidelity 3D models \mathfrak{M}_{3D} :

$$\text{Compare } \mathfrak{M}_{3D}(\theta_{VMR}) \text{ vs. } \mathfrak{M}_{0D}(\theta_{VMR}, \hat{\alpha}) \text{ with } \hat{\alpha} = \arg \min_{\alpha} \|\mathbf{r}(\alpha, \mathfrak{M}_{3D}(\theta_{VMR}))\|^2. \quad (28)$$

We extracted \mathfrak{M}_{3D} velocity and pressure from the last cardiac cycle at all time steps with Windkessel BC parameters θ_{VMR} given from the Vascular Model Repository. Using a previously proposed technique to extract 3D results along the centerline of the blood vessels, we mapped the cross-section

averaged flow rate and pressure from 3D to 0D LPN node points [3, 44]. We initialized the 0D parameters with the values from the geometric model as $\alpha_b^0 = \alpha_b$ and $\alpha_j^0 = \mathbf{0}$ in branches and junctions, respectively. For model 0081_0001, we excluded the stenosis coefficient from LM optimization as the 0D model with optimized stenosis coefficient did not converge during forward evaluations. The optimization of all 72 models took 79s in total on a single core.

Figure 13 in Appendix D provides a detailed correlation of all optimized 0D parameters $\hat{\alpha}_b$ vs. the geometric ones α_b . The mean of the coefficients of determination averaged over all 72 models were $R_R^2 = 0.68$, $R_C^2 = 0.89$, $R_S^2 = 0.23$, and $R_G^2 = 0.24$. This optimization also incorporates 0D junction parameters $\hat{\alpha}_j$. However, since $\alpha_j = \mathbf{0}$ in the geometric 0D models, we cannot provide a correlation for these values. Since we aim to minimize the 0D approximation errors by optimizing element parameters (28), we do not expect the coefficients of determination to be close to one as in Section 3.1.1. Rather, they indicate where the model generation process from a 3D geometry can still be improved. Comparing the optimized parameters $\hat{\alpha}_b$ to the geometric ones α_b in Figure 13, there are some systematic differences. As expected, due to the rigid wall nature of the 3D results, the capacitances \mathcal{C} are optimized as near zero. Furthermore, the optimized stenosis parameters \mathcal{S} are consistently higher, indicating that they are systematically underestimated in the geometric models. However, some pulmonary models with higher post-optimization errors than others exhibit non-zero capacitances \mathcal{C} . Given that these models have many more junctions than others, this could indicate limitations in our **BloodVesselJunction** model in representing 3D fluid dynamics in a junction.

Figure 3 depicts the change in the errors between geometric 0D models $\mathfrak{M}_{0D}(\theta_{VMR}, \alpha_b)$ and optimized 0D models $\mathfrak{M}_{0D}(\theta_{VMR}, \hat{\alpha})$ with respect to 3D models $\mathfrak{M}_{3D}(\theta_{VMR})$. The optimization improved the maximum approximation errors for pressures $\epsilon_{P,\max}$ and flow rates $\epsilon_{Q,\max}$ in 71 out of the 72 models, with error metrics defined as [3]

$$\epsilon_{P,\max} = \frac{n_t}{n_{\text{cap}}} \sum_{i=1}^{n_{\text{cap}}} \frac{\max_t |P_{t,i}^{0D} - P_{t,i}^{3D}|}{\sum_{t=1}^{n_t} P_{t,i}^{3D}}, \quad \epsilon_{Q,\max} = \frac{1}{n_{\text{out}}} \sum_{i=1}^{n_{\text{out}}} \frac{\max_t |Q_{t,i}^{0D} - Q_{t,i}^{3D}|}{\max_t Q_{t,i}^{3D} - \min_t Q_{t,i}^{3D}}, \quad (29)$$

with n_t time steps t , number of outlets n_{out} , and number of caps $n_{\text{cap}} = n_{\text{out}} + 1$. Only the coronary model 0186_0002 performed slightly worse after optimization. For this model, the junction between the aorta and the coronary arteries could not be calibrated properly. Overall, the median error was reduced from 5.6% to 0.6% for pressure and 12.3% to 1.4% for flow following optimization. The optimization achieved the largest improvements for aortofemoral models. Given that our approach optimizes all 0D parameters, it achieves much lower approximation errors than previous studies where only resistances were adapted, e.g., to match key 3D outputs within 10% [13].

Optimizing the 0D models to 3D data lowered their maximum approximation error for pressure and flow rate by nearly one order of magnitude, from $\sim 10\%$ to $\sim 1\%$. This considerable improvement in 0D accuracy is key to our Bayesian Windkessel calibration method. The improvements can be mainly attributed to the optimization of previously unknown **BloodVesselJunction** parameters $\hat{\alpha}_j$. Since the geometric model does not capture the fluid behavior in the junctions, it consistently underestimates their pressure drop. Informing the 0D model using a 3D simulation result, it is easily possible to also derive suitable parameters for the junctions and thereby improve the 0D model to model the full domain accurately.

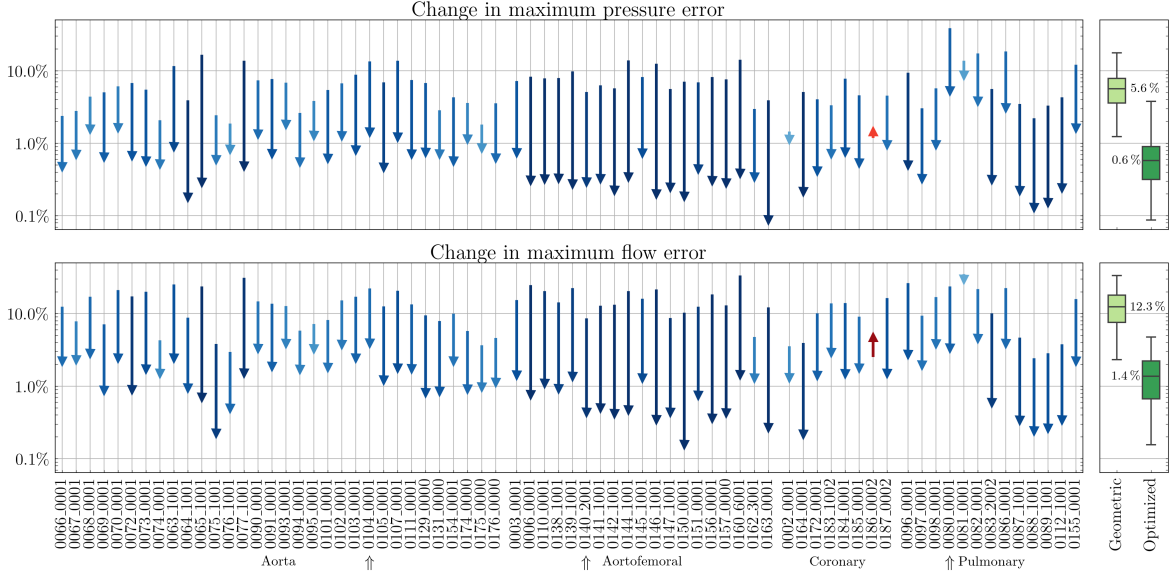


Figure 3: Changes in maximum pressure and flow error between geometric and optimized 0D models. Blue is an improvement; red is a deterioration. Darker values indicate larger changes. Statistical results are provided on the right. See Figure 7 for an overview of the geometries.

3.1.3 Generalization of optimized zero-dimensional models

We demonstrated in Section 3.1.2 that the LM optimization yields 0D models $\mathfrak{M}_{0D}(\theta_{VMR}, \hat{\alpha})$ which reduce maximum pressure and flow errors with respect to 3D models $\mathfrak{M}_{3D}(\theta_{VMR})$ by nearly one order of magnitude compared to geometric models $\mathfrak{M}_{0D}(\theta_{VMR}, \alpha_b)$ for fixed Windkessel parameters θ_{VMR} . In this section, we demonstrate that 0D models $\mathfrak{M}_{0D}(\theta_v, \hat{\alpha})$ optimized with Windkessel training parameters θ_t generalize well to a wide range of Windkessel validation parameters θ_v :

$$\text{Compare } \mathfrak{M}_{3D}(\theta_v) \text{ vs. } \mathfrak{M}_{0D}(\theta_v, \hat{\alpha}) \text{ with } \hat{\alpha} = \arg \min_{\alpha} \|\mathbf{r}(\alpha, \mathfrak{M}_{3D}(\theta_t))\|^2, \quad \theta_v \neq \theta_t. \quad (30)$$

This generalization is crucial to our goal of using 0D models as a surrogate in Bayesian Windkessel calibration. If optimized 0D models generalize well over a wide range of Windkessel parameters θ , we can confidently approximate the posterior distribution $\mathbf{p}_{3D} \approx \mathbf{p}_{0D}$.

Since this generalization study requires extensive sampling of computationally expensive 3D simulation results, we select a subset of three simulation models: the aortic model of an 11-year-old human female with aortic coarctation 0104_0001, the aortofemoral model of a 76-year-old human male with an abdominal aortic aneurysm 0140_2001, and the pulmonary model of a 43-year-old healthy human female 0080_0001. See Figure 7 for their geometries. These models span three different anatomies and exhibit high pressure and flow approximation errors of the geometric 0D models of around 10%, highlighted with arrows in Figure 3. For each model, we reused a set $\{\theta_i\}$ of 50 variations of BC parameters from Pegolotti et al. [47]. This dataset was generated by multiplying flow rates, resistance, and capacitance values of the BCs parameters by a factor randomly and independently sampled from a uniform distribution between 0.8 and 1.2. In each comparison, we used identical BC parameters θ_i in geometric 0D models $\mathfrak{M}_{0D}(\theta_i, \alpha_b)$ and optimized ones $\mathfrak{M}_{0D}(\theta_i, \hat{\alpha})$ and compared them to the corresponding 3D models $\mathfrak{M}_{3D}(\theta_i)$. To ensure comparability, we applied the 3D result of the first time step in the last simulated cardiac cycle as initial conditions to the 0D simulation. The 0D models were then evaluated for one cardiac cycle to ensure that the cardiac cycles in 0D and 3D were identical.

For each validation, we optimized the 0D model to one BC training parameter set θ_t and compared approximation errors for all other 49 BC validation parameters θ_v :

$$\theta_{t,i} = \theta_i, \quad \theta_{v,i} = \{\theta_1, \dots, \theta_{50}\} \setminus \theta_i, \quad \forall i \in \{1, \dots, 50\}. \quad (31)$$

We perform this validation fifty times to obtain a cross-validation. Figure 4 shows the cross-validation error at systole for pressure and flow. The performance of the optimized model is further divided

into performance on the training set $\{\theta_{t,i}\}$ and the validation set $\{\theta_{v,i}\}$. For reference, we also show errors for the geometric 0D model, i.e., without optimization. There is a large variance of errors for the geometric model evaluated on all $|\{\theta_i\}| = 50$ BCs parameter sets. As observed in Section 3.1.2, the error is drastically reduced on the training set of all three optimized 0D models. Furthermore, the variance of the $|\{\theta_{t,i}\}| = 50$ training errors is much lower. Most importantly, the validation error is equal to or slightly larger than the training error. Despite encompassing $|\{\theta_{v,i}\}| = 50 \times 49 = 2450$ simulations, the variance of the validation error is only slightly larger than the one of the 50 training errors.

We summarize two observations: First, although the optimized pulmonary models have been significantly improved, they perform worse than the aortic models. This could be related to the increased size and, thus, the complexity of the model but could also hint toward a limitation of the junction model used herein, as junctions make up a large portion of the pulmonary model domain. Second, we do not observe a notable difference in the low 0D model error from Section 3.1.2 even for randomly sampled BC parameters. This confirms good generalization of the LM optimization approach, which demonstrates that we can confidently use the approximation $\mathfrak{M}_{3D}(\theta) \approx \mathfrak{M}_{0D}(\theta, \hat{\alpha})$ for the Bayesian Windkessel BC calibration in Section 3.2.

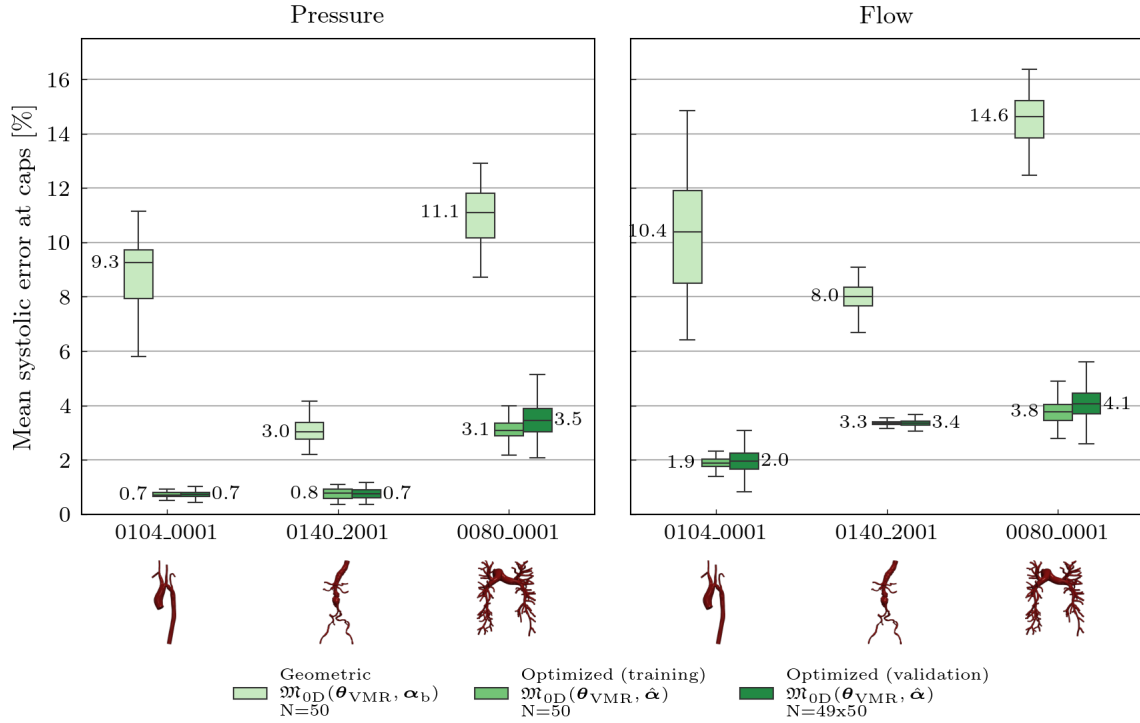


Figure 4: Cross-validation of optimized 0D model $\mathfrak{M}_{0D}(\theta_{VMR}, \hat{\alpha})$ and comparison to geometric 0D model $\mathfrak{M}_{0D}(\theta_{VMR}, \alpha_b)$. In each validation, the model was calibrated to the test parameters, and the result was compared to the 49 validation parameters.

3.2 Bayesian Windkessel calibration incorporating optimized zero-dimensional models

This section applies the BC calibration approach proposed in Section 2.1 to the aortic model of an 11-year-old human female with aortic coarctation 0104.0001. We split this section into problem-setup (3.2.1), results (3.2.2), and validation (3.2.3).

3.2.1 Problem setup

Our problem setup is typical for cardiovascular fluid dynamics simulations and is often performed manually or according to well-known heuristics. Typical flow measurements are obtained from 4D Flow Magnetic Resonance Imaging at the inlet and outlets of the model [48]. Pressure measurements at the inlet are obtained either from *in vivo* catheter measurements or estimated from cuff measurements [49].

In this section, one BC parameter denoted as $\theta^{(i)}$ is calibrated for each outlet (i.e., each Windkessel) of the model. The parameter $\theta^{(i)}$ is the logarithmic total resistance at the respective Windkessel outlet

$$\theta^{(i)} = \log(R^{(i)}), \quad R^{(i)} = R_p^{(i)} + R_d^{(i)}. \quad (32)$$

The logarithmic reparameterization ensures that the resistances remain positive, independent of the parameter choice, as negative resistances are unphysiological and usually lead to failed forward model evaluations. This yields the overall parameter vector

$$\boldsymbol{\theta} = [\log(R^{(1)}), \dots, \log(R^{(n_{\text{out}})})]^\top, \quad (33)$$

with the number of outlets n_{out} . The individual parameters of each Windkessel model, i.e., R_p , R_d , and C , are derived from the total resistance based on two assumptions: The ratio between distal to proximal resistance is assumed as constant and given

$$\frac{R_{p,i}}{R_{d,i}} = \text{const}, \quad (34)$$

and the time constant τ_i of each Windkessel BC is known and constant

$$\tau_i = R_{d,i} \cdot C_i = \text{const}. \quad (35)$$

The respective values for τ_i and $R_{p,i}/R_{d,i}$ are calculated based on the existing BC parameters $\boldsymbol{\theta}_{\text{VMR}}$ in the Vascular Model Repository. In practice, they would be estimated from the total resistance and total capacitance of the vasculature represented by the BCs. However, our approach can also be used in other scenarios, e.g., simultaneously estimating capacitance C_i and resistance ratio $R_{p,i}/R_{d,i}$ for each outlet [4]. The observations \mathbf{y}_{obs} for this example are artificially created based on one 3D simulation for the geometry with BC parameters $\boldsymbol{\theta}_{\text{VMR}}$. In agreement with typical clinical measurements, the following observations have been selected: the minimum pressure at the inlet, the maximum pressure at the inlet, and the time-averaged flow rates at each outlet

$$\mathbf{y}_{\text{obs}} = [P_{\text{in,min}}, P_{\text{in,max}}, Q_{\text{mean,1}}, \dots, Q_{\text{mean},n_{\text{outlets}}}]^\top. \quad (36)$$

The aortic anatomy 0104.0001 has five outlets connected to Windkessel BCs and accordingly five calibration parameters $\theta^{(i)}$ and seven observations $y_{\text{obs}}^{(i)}$. It is assumed that the observations are corrupted by additive Gaussian noise as specified in Section 2.1.2, which is characterized by a constant signal-to-noise ratio

$$\text{SNR}_i = \frac{y_{\text{obs},i}^2}{\sigma_i^2} = \text{const}, \quad (37)$$

for all observations $y_{\text{obs},i}$.

3.2.2 Posterior distribution for Windkessel boundary conditions

The Bayesian Windkessel calibration is performed with three signal-to-noise ratios of 100, 11.1, and 4 to investigate changes in the posterior distribution for increasing noise in observations \mathbf{y}_{obs} . SMC is performed with $k = 10\,000$ particles, a resampling threshold $\text{ESS}_{\text{min}} = 5\,000$, and two rejuvenation steps per iteration. All calculations were performed on Stanford's high performance computing cluster Sherlock using four 12-core Intel Xeon Gold 5118 CPUs. It should be noted, however, that only the 3D simulation took advantage of all 48 available cores. We ran the SMC algorithm on 24 cores and the LM calibration on a single core. The parameter estimation for the $\text{SNR} = 100$ case took a bit over 24h, where 1.5h was spent on the first SMC run (with 210 000 0D evaluations), 21.5h on the 3D simulation and 1.5h on the second SMC run. The LM calibration took only 20s.

Figure 5 presents the posterior densities for all parameters $\theta^{(i)}$ and signal-to-noise ratios SNR. All parameter distributions are concentrated around single values for the high signal-to-noise ratio SNR = 100. The locations of the peaks match well with the parameter values used to create the artificial observations (marked by the crossing gray lines). The posterior variance is low, which matches the expectation given that the noise in observations is low. The posterior variance is generally larger for the lower single-to-noise ratio SNR = 11.1, and some distributions exhibit multi-modality. The posterior distributions for the BC parameter at the descending aorta $\theta^{(2)}$ are narrower compared to the other parameters, suggesting a higher sensitivity of the model output to $\theta^{(2)}$. For the largest noise case SNR = 4, the posterior is characterized by the largest variance.

The results show that the proposed Bayesian calibration approach successfully captured the multi-dimensional posterior distribution of the Windkessel parameters based on the optimized 0D model $\mathfrak{M}_{0D}(\theta_{VMR}, \hat{\alpha})$ and delivered robust results even for completely uninformed and broad priors. It has been demonstrated that the Bayesian calibration approach is advantageous in settings where observations are corrupted with noise. While the posterior collapses almost to a Dirac distribution in the case of a high signal-to-noise ratio in the observations, the cases with high measurement noise highlight how the uncertainty propagates to the posterior.

Calculating the full posterior distribution provides many advantages compared to deterministic optimization strategies, where only a point estimate is obtained. First, the probabilistic calibration problem is better posed and less prone to get stuck in local optima. Second, the posterior distribution provides a quantification of confidence in the calibration result. This is instrumental for future clinical application of these models as it allows one to assess the expected reliability of a simulation model calibrated based on very sparse data. Knowing the full posterior distribution allows for more nuanced and better-informed parameter choices. Third, the posterior distributions can be used to quantify uncertainty in model predictions using forward propagation, e.g., wall shear stress in thoracic aortic aneurysms [50] or pressure drop over an aortic coarctation [51]. In the latter, the uncertainty in the model prediction can be taken into account while making the clinical decision of whether to intervene or not [4]. We enabled the sampling intensive SMC algorithm by developing a fast `svZeroDSolver` that performed the hundreds of thousand 0D evaluations in a bit over an hour.

3.2.3 Comparison of 0D posterior with 3D posterior

The framework proposed in Section 2.1 relies on the assumption that 0D models $\mathfrak{M}_{0D}(\theta, \hat{\alpha})$ with optimized 0D parameters $\hat{\alpha}$ approximate the 3D model $\mathfrak{M}_{3D}(\theta)$ accurately. This was demonstrated in a deterministic sense in Section 3.1 for a wide range of Windkessel BC parameters θ . In this section, we validate that a posterior distribution based on an optimized 0D model $p_{0D}(\mathbf{y}_{obs}|\theta, \hat{\alpha})$ agrees with the posterior distributions based on the full-dimensional 3D model $p_{3D}(\mathbf{y}_{obs}|\theta)$ given identical uncertain observations \mathbf{y}_{obs} .

To ensure computational feasibility, we reduce the problem setup from Sections 3.2.1 and 3.2.2 to two dimensions. The parameters $\theta^{(1)}$, $\theta^{(2)}$, $\theta^{(4)}$ and $\theta^{(5)}$ are now coupled and denoted as $\theta^{(1,2,4,5)}$ in the following and $\theta^{(3)}$ is calibrated individually. We evaluate the unnormalized posterior point-wise on a uniform 10x10 grid in the interval [2, 8] for $\theta^{(1,2,4,5)}$ and [3, 6] for $\theta^{(3)}$ on a geometric 0D model $\mathfrak{M}_{0D}(\alpha_b)$, an optimized 0D model $\mathfrak{M}_{0D}(\hat{\alpha})$, and a full-dimensional 3D model \mathfrak{M}_{3D} . Afterward, we normalize the unnormalized posterior to yield an estimate of the true posterior distribution. A signal-to-noise ratio of SNR = 11.1% is used. Performing all 100 3D simulations took nearly 800 hours on two 64-core AMD EPYC 7742 CPUs, while the 100 0D simulations were completed in less than a minute on a single core.

The resulting posterior distributions for the three models are presented in Figure 6. The geometric and optimized 0D models exhibit more posterior variance than the 3D model. While the geometric 0D model posterior shows no overlap with the 3D posterior, the optimized 0D model has a much-improved agreement with the latter. Despite the slight elongation of the posterior for the 0D models, 3D and optimized 0D models attribute most of the probability mass in a similar region close to the coordinate (6, 5). As seen in Section 3.1.2, model 0104.0001 was intentionally selected as one of the worst-performing 0D models. However, it still achieved a good approximation of the 3D posterior, especially compared to the geometric 0D model, with a tendency to overestimate the uncertainty in the calibration result.

The optimized 0D posterior deviates slightly from the high-fidelity 3D posterior but clearly encapsulates the latter. In contrast, the geometric 0D model completely fails to provide a viable surrogate

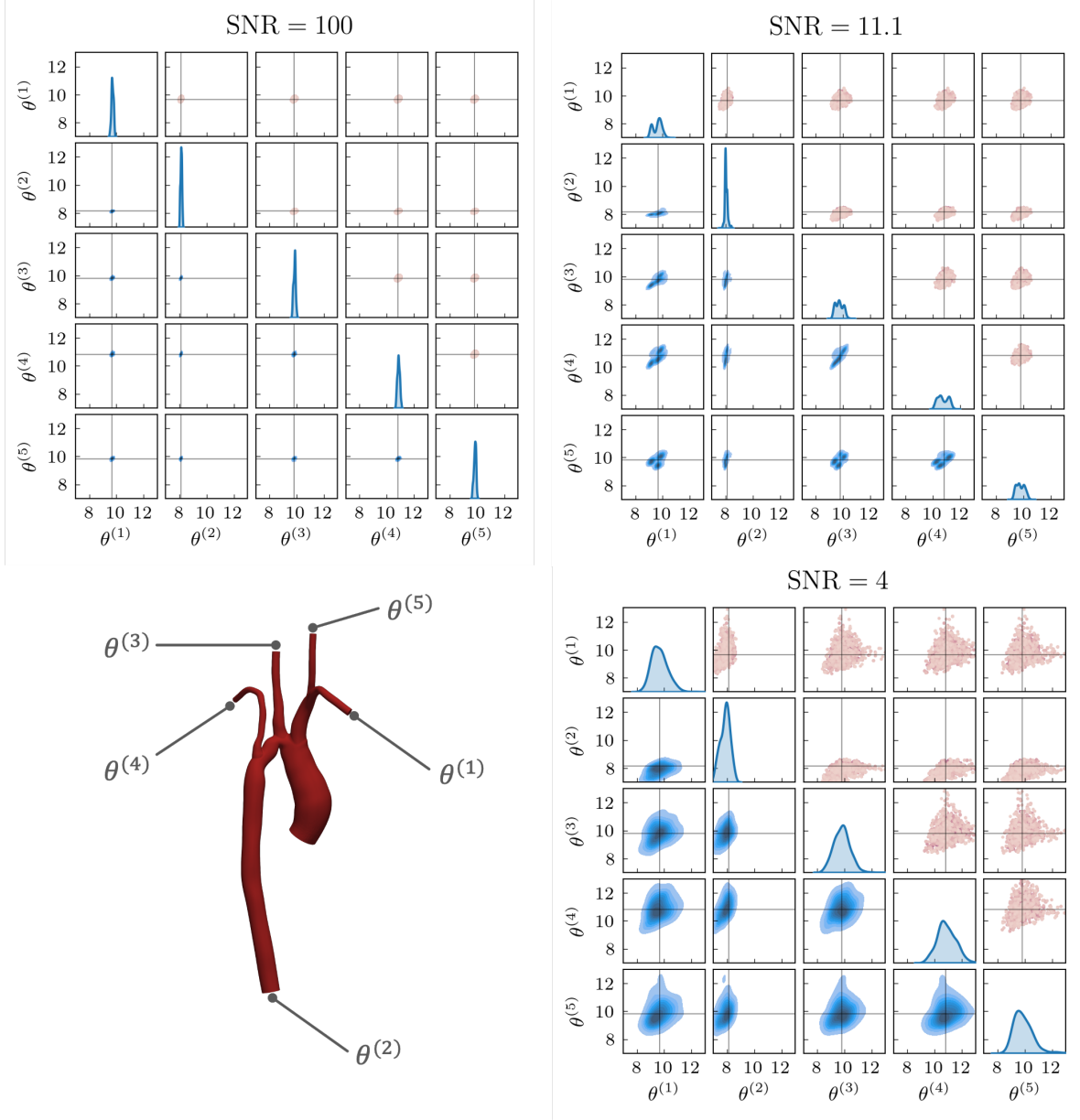


Figure 5: 2D marginals of the 5D posterior for all parameters $\theta^{(i)}$ and signal-to-noise ratios SNR based on model 0104.0001. The diagonal plots show the 1D kernel density estimate. The upper right plots the particles colored by their weight, and the lower left plots the 2D density contours. The parameter values corresponding to the ground truths are marked with crossing gray lines.

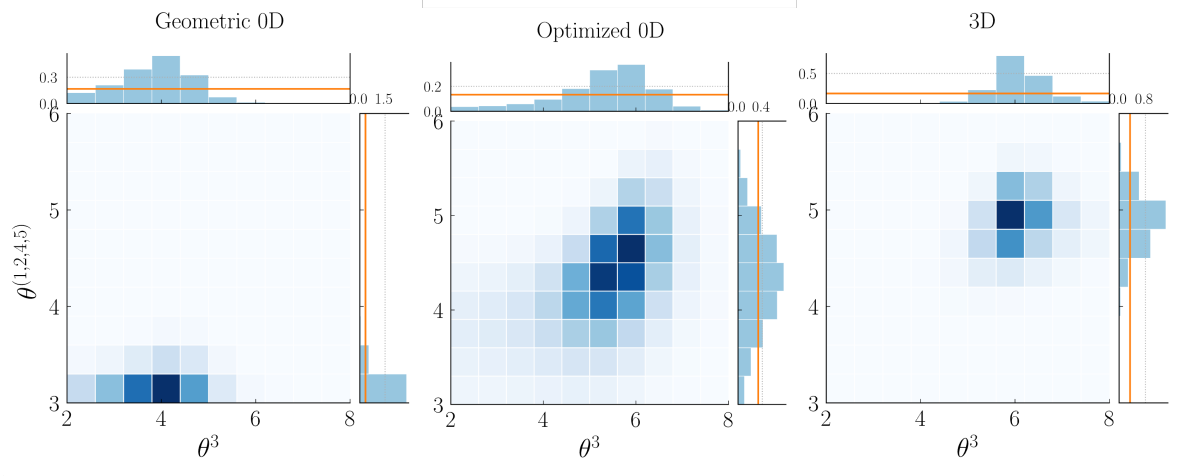


Figure 6: Comparison of the posterior distribution evaluated on the geometric 0D model, the calibrated 0D model, and the 3D model. The uniform prior is added in orange to the marginal distributions.

for the 3D posterior. While the geometric 0D model attributes the majority of its probability density to wrong parameter choices and, thus, provides confidence in incorrect results, the optimized 0D model merely overpredicts the posterior variance. This discrepancy is due to the residual 0D-3D approximation error after optimization. Informing the 0D model by a single 3D simulation result was sufficient to increase the agreement between 0D model and 3D model to the extent that the 0D model can confidently be used for parameter calibration without requiring further 3D evaluations. These results confirm that the optimized 0D models are not only superior to the geometric 0D models for approximating the 3D posterior but are essential. Moreover, it has been confirmed that the approach proposed in this work allows for accurate and efficient probabilistic parameter calibration for Windkessel BCs.

4 Limitations and outlook

We demonstrated that a LM optimization approach can derive highly accurate 0D models based on a 3D simulation of a single heartbeat. The optimized 0D models showed great agreement with the physiological behavior of 3D models even during substantial changes in the BCs. The optimization also proved effective for automatically determining parameters for 0D junctions, which is a known challenge for cardiovascular reduced-order models. The results provide valuable insights regarding the potential to improve the automatic creation of LPN models. This could be used to develop more accurate 0D element parameters that are informed by both geometry and hemodynamics or as training data for machine-learning-based approaches to 0D model generation [40].

Despite the significant reduction in 0D-3D approximation errors, there are still some deviations between the optimized 0D models and the 3D models, especially for pulmonary models. While it is not possible to achieve perfect agreement between 3D and 0D models, this indicates that improvements to the 0D models themselves may need to be investigated to include more nonlinear terms that better capture 3D flow physics. A structured analysis of the physiological effects currently not accounted for by the 0D elements could result in better agreement. Additionally, a probabilistic optimization approach could provide more information about the identifiability of the individual 0D parameters based on the 3D training data. The 0D model optimization has been performed using one cardiac cycle of a periodically converged simulation. Future studies should investigate whether the amount of 3D data necessary to sufficiently inform the 0D model optimization can be further reduced, i.e., a few 3D time steps may suffice. This would reduce the computational expense of the algorithm even further.

We demonstrated that optimized 0D models can be deployed for accurate and efficient Bayesian Windkessel calibration using SMC. While the optimized 0D posterior slightly overestimates uncertainty compared to the ground-truth 3D posterior, it significantly adds more nuance than the state-of-the-art

deterministic calibration. The Bayesian approach not only provides more robustness for the calibration, but the resulting posterior distributions also provide a powerful tool for making more informed parameter decisions in patient-specific cardiovascular modeling. While deterministic calibration results can only be interpreted in one way (as the final parameter choice), the posterior distributions can be processed to retrieve the optimal parameter choice in view of multiple aspects (e.g. risk-assessment, feasibility analysis). The posterior also provides additional information about the uncertainty in the parameters given potentially noisy clinical measurements. This is especially relevant in a clinical setting where data is usually sparse and noisy. The results can also be used to decide whether a parameter choice can be made confidently based on the given clinical measurement or if more data is required.

We evaluated the proposed calibration framework on artificially created measurement data. While the problem setup aimed to match a common calibration scenario, further work could focus on using subject data. Applying the proposed calibration framework to different setups can validate its robustness on realistic clinical data. Moreover, we limited our investigations to rigid-wall 3D models of the vasculature. While this is a valid assumption for the stiffer vasculature or lower pressures, it is not generally applicable. Nevertheless, despite wall compliance being near zero, we demonstrated that our 0D parameter optimization can robustly identify vessel capacity. Further, we demonstrated that our forward and inverse 0D models can incorporate vessel wall elasticity and highlighted differences between rigid and compliant wall pressure curves in a previous publication [3]. We thus expect that our calibration framework will be applicable to compliant-wall simulations as well.

The posterior distribution derived based on the optimized 0D models has been compared against the high-fidelity 3D posterior and proved to be a valid surrogate for the latter. The poor performance of the geometric 0D model highlighted that the 0D-3D optimization is essential for performing Bayesian calibration on 0D models. Our framework can be improved by incorporating more than one high-fidelity 3D simulation in clinical scenarios that require a more accurate calibration. A multi-fidelity approach could model the 0D-3D discrepancy to generate a more accurate surrogate for the 3D model [12, 17, 27, 28]. Alternatively, further work could generalize the algorithm presented herein using an expectation-maximization approach that treats the 0D model parameters α as latent variables that are consistently optimized as part of the inverse problem. This algorithm has guaranteed convergence properties under certain conditions and would allow for a more robust Bayesian 0D parameter optimization. This full Bayesian treatment also allows to quantify the uncertainty of the 0D parameter optimization within the BC calibration.

Acknowledgements

This work was supported by grants K99HL161313, R01HL167516, and R01HL141712 from the National Heart, Lung, and Blood Institute and the Stanford Maternal and Child Health Research Institute. DES acknowledges partial support from NSF CAREER award #1942662 and NSF CDS&E award #2104831. WAW and JN acknowledge support from the European Research Council (grant agreement No. 101021526-BREATHE). The authors gratefully acknowledge the Stanford Research Computing Center and the San Diego Super Computing Center (SDSC) Expanse cluster for providing the computational resources necessary for the numerical simulations presented in this work.

A Overview of cardiovascular models

Figure 7 shows an overview of all 72 models used in this work, identical to the ones in Pfaller et al. [3]. They are openly available from the Vascular Model Repository [46].

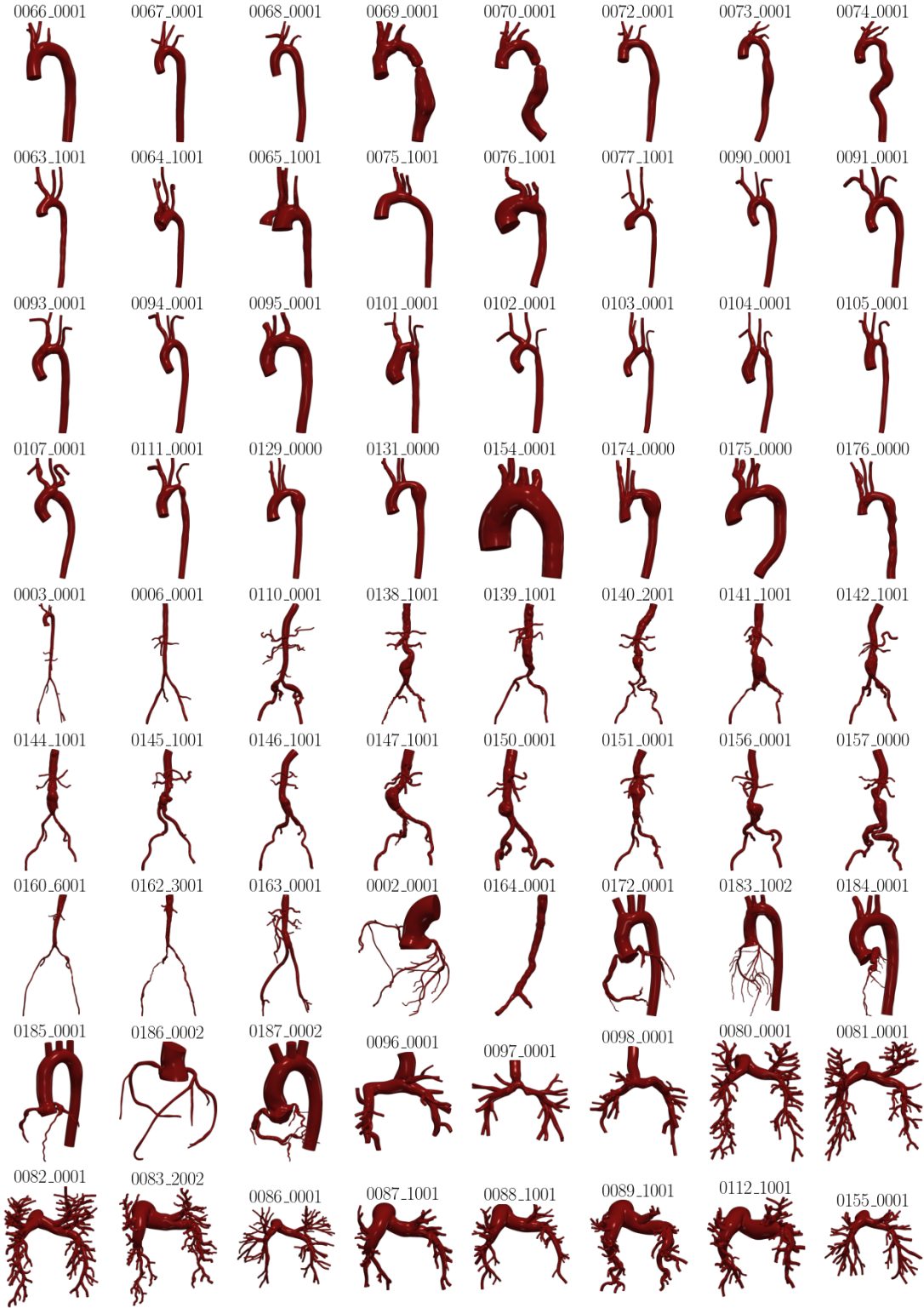


Figure 7: Overview of models used in this work, sorted by anatomy. This set is identical to the one in Pfaller et al. [3].

B Computational details of zero-dimensional models

This section contains the zero-dimensional (0D) time integration scheme (B.1) and the system matrices for the `BloodVessel` (B.3), `BloodVesselJunction` (B.4), and `Windkessel` (B.5) lumped-parameter network elements as implemented in `svZeroDSolver` [43].

B.1 Forward time integration

We use a generalized- α time integration [52, 53] and solve for the solution vector \mathbf{y} in each time step n using the Newton-Raphson method,

$$\text{Predict: } \dot{\mathbf{y}}_{n+1}^0 = \frac{\gamma - 1}{\gamma} \dot{\mathbf{y}}_n, \quad (38)$$

$$\mathbf{y}_{n+1}^0 = \mathbf{y}_n, \quad (39)$$

$$\text{Initiate: } \dot{\mathbf{y}}_{n+\alpha_m}^i = \dot{\mathbf{y}}_n + \alpha_m (\dot{\mathbf{y}}_{n+1}^i - \dot{\mathbf{y}}_n), \quad (40)$$

$$\mathbf{y}_{n+\alpha_f}^i = \mathbf{y}_n + \alpha_f (\mathbf{y}_{n+1}^i - \mathbf{y}_n), \quad (41)$$

$$\text{Solve: } \mathbf{K}(\mathbf{y}_{n+\alpha_f}^i, \dot{\mathbf{y}}_{n+\alpha_m}^i) \cdot \Delta \dot{\mathbf{y}}_{n+1}^i = -\mathbf{r}(\mathbf{y}_{n+\alpha_f}^i, \dot{\mathbf{y}}_{n+\alpha_m}^i), \quad (42)$$

$$\text{Update: } \dot{\mathbf{y}}_{n+1}^{i+1} = \dot{\mathbf{y}}_{n+1}^i + \Delta \dot{\mathbf{y}}_{n+1}^i, \quad (43)$$

$$\mathbf{y}_{n+1}^{i+1} = \mathbf{y}_{n+1}^i + \Delta \dot{\mathbf{y}}_{n+1}^i \gamma \Delta t_n, \quad (44)$$

with time step Δt_n , residual \mathbf{r} , and Jacobian \mathbf{K} . We derive the generalized- α parameters α_f , α_m , and γ from the spectral radius ρ_∞

$$\alpha_m = \frac{1 - \rho_\infty}{2(1 + \rho_\infty)}, \quad \alpha_f = \frac{1}{1 + \rho_\infty}, \quad \gamma = \frac{1}{2} + \alpha_m - \alpha_f. \quad (45)$$

B.2 Inverse parameter optimization

We use the Levenberg-Marquardt (LM) algorithm [54, 55] to solve the least squares problem (25) iteratively for the optimal parameter set $\hat{\boldsymbol{\alpha}}$,

$$\text{update } \boldsymbol{\alpha}^{i+1} = \boldsymbol{\alpha}^i + \Delta \boldsymbol{\alpha}^{i+1}, \quad (46)$$

$$\text{solve } [\mathbf{J}^T \mathbf{J} + \lambda \text{diag}(\mathbf{J}^T \mathbf{J})]^i \cdot \Delta \boldsymbol{\alpha}^{i+1} = -[\mathbf{J}^T \mathbf{r}]^i, \quad \lambda^i = \lambda^{i-1} \cdot \frac{\|[\mathbf{J}^T \mathbf{r}]^i\|_2}{\|[\mathbf{J}^T \mathbf{r}]^{i-1}\|_2}. \quad (47)$$

The LM algorithm approximates the Hessian from the Jacobian matrix \mathbf{J} as $\Delta S \approx \mathbf{J}^T \mathbf{J}$. The second term introduces damping with factor λ , which we update based on the change in gradient $\nabla S = \mathbf{J}^T \mathbf{r}$. Thus, the damping parameter approaches $\lambda \rightarrow 0$ as the parameter set $\boldsymbol{\alpha} \rightarrow \hat{\boldsymbol{\alpha}}$ approaches the optimal solution. For $\lambda \rightarrow \infty$, we obtain the steepest descent method, and for $\lambda = 0$, we obtain the Gauss-Newton method. We terminate the optimization (47) when both L^2 norms,

$$\|[\mathbf{J}^T \mathbf{r}]^i\|_2 < \text{tol}_{\text{grad}}^\alpha \text{ and } \|\Delta \boldsymbol{\alpha}^{i+1}\|_2 < \text{tol}_{\text{inc}}^\alpha, \quad (48)$$

are below the tolerances for gradient and increment, $\text{tol}_{\text{grad}}^\alpha$ and $\text{tol}_{\text{inc}}^\alpha$, respectively. In this work, we chose the LM optimization parameters of initial damping factor $\lambda^0 = 1$, gradient tolerance $\text{tol}_{\text{grad}}^\alpha = 10^{-5}$, increment tolerance $\text{tol}_{\text{inc}}^\alpha = 10^{-10}$, and a maximum number of iterations of 100.

B.3 BloodVessel element

We model the blood vessel branches with the `BloodVessel` element, whose circuit is visualized in Figure 8.

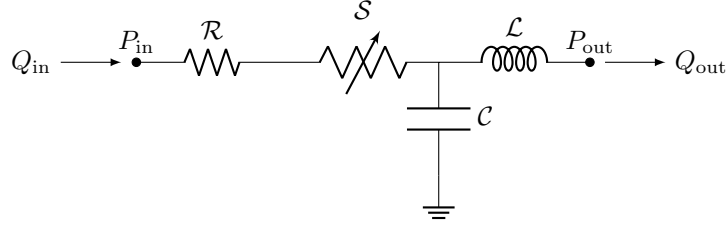


Figure 8: The **BloodVessel** element with resistance \mathcal{R} , stenosis \mathcal{S} , inertance \mathcal{L} , and capacitance \mathcal{C} .

The governing equations are given by

$$-(\mathcal{R} + \mathcal{S}|Q_{\text{in}}|) Q_{\text{in}} - \mathcal{L} \dot{Q}_{\text{out}} - \Delta P = 0, \quad (49)$$

$$\mathcal{C}(\mathcal{R} + 2\mathcal{S}|Q_{\text{in}}|) \dot{Q}_{\text{in}} - \mathcal{C} \dot{P}_{\text{in}} - \Delta Q = 0. \quad (50)$$

The remainder of this section contains the forward (B.3.1) and inverse (B.3.2) problem of the **BloodVessel** element.

B.3.1 Forward problem

The vector of element unknowns is

$$\mathbf{y}^{(e)} = \begin{bmatrix} P_{\text{in}}^{(e)} & Q_{\text{in}}^{(e)} & P_{\text{out}}^{(e)} & Q_{\text{out}}^{(e)} \end{bmatrix}^T \quad (51)$$

The **BloodVessel** element matrices for the forward problem (19) are

$$\mathbf{E}^{(e)} = \begin{bmatrix} 0 & 0 & 0 & -\mathcal{L} \\ -\mathcal{C} & \mathcal{C}\mathcal{R} & 0 & 0 \end{bmatrix}^{(e)}, \quad (52)$$

$$\mathbf{F}^{(e)} = \begin{bmatrix} 1 & -\mathcal{R} & -1 & 0 \\ 0 & 1 & 0 & -1 \end{bmatrix}^{(e)}, \quad (53)$$

$$\mathbf{c}^{(e)} = \mathcal{S}|Q_{\text{in}}| \begin{bmatrix} -Q_{\text{in}} \\ 2\mathcal{C}\dot{Q}_{\text{in}} \end{bmatrix}^{(e)}. \quad (54)$$

Only the stenosis term \mathcal{S} contributes to the nonlinear term \mathbf{c} . Its linearizations are

$$\left(\frac{\partial \mathbf{c}}{\partial \dot{\mathbf{y}}} \right)^{(e)} = \mathcal{S}|Q_{\text{in}}| \begin{bmatrix} 0 & 0 & 0 & 0 \\ 0 & 2\mathcal{C} & 0 & 0 \end{bmatrix}^{(e)}, \quad (55)$$

$$\left(\frac{\partial \mathbf{c}}{\partial \mathbf{y}} \right)^{(e)} = \mathcal{S} \text{sgn}(Q_{\text{in}}) \begin{bmatrix} 0 & -2Q_{\text{in}} & 0 & 0 \\ 0 & 2\mathcal{C}\dot{Q}_{\text{in}} & 0 & 0 \end{bmatrix}^{(e)}. \quad (56)$$

B.3.2 Inverse problem

The vector of element unknowns is

$$\boldsymbol{\alpha}^{(e)} = \begin{bmatrix} \mathcal{R}^{(e)} & \mathcal{C}^{(e)} & \mathcal{L}^{(e)} & \mathcal{S}^{(e)} \end{bmatrix}^T, \quad (57)$$

containing flow and pressure for the inlet and n outlets. The **BloodVessel** element Jacobian matrix for the inverse problem (24) is

$$\mathbf{J}^{(e)} = \begin{bmatrix} -Q_{\text{in}} & 0 & -\dot{Q}_{\text{out}} & -|Q_{\text{in}}|Q_{\text{in}} \\ \mathcal{C}\dot{Q}_{\text{in}} & -\dot{P}_{\text{in}} + (\mathcal{R} + 2\mathcal{S}|Q_{\text{in}}|)\dot{Q}_{\text{in}} & 0 & 2\mathcal{C}|Q_{\text{in}}|\dot{Q}_{\text{in}} \end{bmatrix}^{(e)}. \quad (58)$$

B.4 BloodVesselJunction element

We model the junctions between blood vessel branches with the **BloodVesselJunction** element. It is visualized in Figure 9 (top) for an inlet connecting to $1, \dots, n$ outlets. An individual junction model connecting the inlet to outlet i is visualized in Figure 9 (bottom).

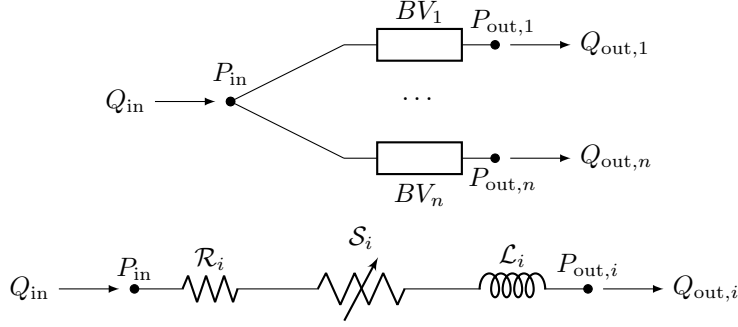


Figure 9: The **BloodVesselJunction** element (top), connecting an inlet to n outlets. An individual inlet-outlet connection BV_i is shown at the bottom, with resistance \mathcal{R}_i , stenosis \mathcal{S}_i , and inductance \mathcal{L}_i .

The governing equations for the **BloodVesselJunction** are

$$Q_{\text{in}} - \sum_i^n Q_{\text{out},i} = 0, \quad (59)$$

$$\Delta P_i + (\mathcal{R} + \mathcal{S}|Q_{\text{out},i}|) Q_{\text{out},i} + \mathcal{L} \dot{Q}_{\text{out},i} = 0, \quad \forall i = 1, \dots, n. \quad (60)$$

The remainder of this section contains the forward (B.4.1) and inverse (B.4.2) problem of the **BloodVesselJunction** element.

B.4.1 Forward problem

The vector of element unknowns is

$$\mathbf{y}^{(e)} = \begin{bmatrix} P_{\text{in}}^{(e)} & Q_{\text{in}}^{(e)} & P_{\text{out},1}^{(e)} & Q_{\text{out},1}^{(e)} & P_{\text{out},2}^{(e)} & Q_{\text{out},2}^{(e)} & \dots \end{bmatrix}^T. \quad (61)$$

The **BloodVesselJunction** element matrices for the forward problem (19) are

$$\mathbf{E}^{(e)} = \begin{bmatrix} 0 & 0 & 0 & 0 & 0 & 0 & \dots \\ 0 & 0 & 0 & -\mathcal{L}_1 & 0 & 0 & \\ 0 & 0 & 0 & 0 & 0 & -\mathcal{L}_2 & \\ \vdots & & & & & & \ddots \end{bmatrix}^{(e)}, \quad (62)$$

$$\mathbf{F}^{(e)} = \begin{bmatrix} 0 & 1 & 0 & -1 & 0 & -1 & \dots \\ 1 & 0 & -1 & -\mathcal{R}_1 & 0 & 0 & \\ 1 & 0 & 0 & 0 & -1 & -\mathcal{R}_2 & \\ \vdots & & & & & & \ddots \end{bmatrix}^{(e)}, \quad (63)$$

$$\mathbf{c}^{(e)} = \begin{bmatrix} 0 \\ -\mathcal{S}_1 |Q_{\text{in},1}| Q_{\text{in},1} \\ -\mathcal{S}_2 |Q_{\text{in},2}| Q_{\text{in},2} \\ \vdots \end{bmatrix}^{(e)}, \quad (64)$$

with the first rows in each component containing the conservation of mass equation (59). The linearization of the nonlinear term \mathbf{c} is

$$\left(\frac{\partial \mathbf{c}}{\partial \dot{\mathbf{y}}} \right)^{(e)} = \mathbf{0}, \quad (65)$$

$$\left(\frac{\partial \mathbf{c}}{\partial \mathbf{y}} \right)^{(e)} = 2 \begin{bmatrix} 0 & 0 & 0 & 0 & 0 & 0 & \dots \\ 0 & 0 & 0 & -\mathcal{S}_1 |Q_{\text{in},1}| & 0 & 0 & \\ 0 & 0 & 0 & 0 & 0 & -\mathcal{S}_1 |Q_{\text{in},2}| & \\ \vdots & & & & & & \ddots \end{bmatrix}^{(e)}. \quad (66)$$

B.4.2 Inverse problem

The vector of element unknowns is

$$\boldsymbol{\alpha}^{(e)} = \left[\mathcal{R}_1^{(e)} \quad \mathcal{R}_2^{(e)} \quad \dots \quad \mathcal{L}_1^{(e)} \quad \mathcal{L}_2^{(e)} \quad \dots \quad \mathcal{S}_1^{(e)} \quad \mathcal{S}_2^{(e)} \quad \dots \right]^T, \quad (67)$$

consisting of $3n$ unknowns for a junction with n outlets. The `BloodVesselJunction` element Jacobian matrix for the inverse problem (24) is

$$\mathbf{J}^{(e)} = \begin{bmatrix} 0 & 0 & \dots & 0 & 0 & \dots & 0 & 0 & \dots \\ -Q_{\text{out},1} & 0 & & -\dot{Q}_{\text{out},1} & 0 & & |Q_{\text{in},1}| Q_{\text{in},1} & 0 & \\ 0 & -Q_{\text{out},2} & & 0 & -\dot{Q}_{\text{out},2} & & 0 & |Q_{\text{in},2}| Q_{\text{in},2} & \\ \vdots & & \ddots & \vdots & & \ddots & \vdots & & \ddots \end{bmatrix}^{(e)}. \quad (68)$$

B.5 Windkessel element

We use a three-element Windkessel visualized in Figure 10.

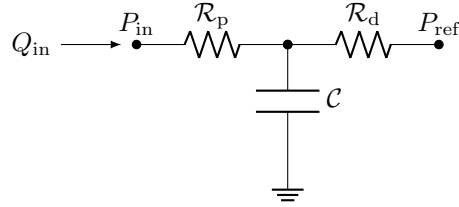


Figure 10: Three-element `Windkessel` boundary condition (BC)

It is governed by the equation

$$(\mathcal{R}_p + \mathcal{R}_d) Q_{\text{in}} - P_{\text{in}} + P_{\text{ref}} - \mathcal{R}_d C \dot{P}_{\text{in}} + \mathcal{R}_p \mathcal{R}_d \dot{Q}_{\text{in}} = 0. \quad (69)$$

consisting of a capacitance \mathcal{C} , and proximal and distal resistances \mathcal{R}_p and \mathcal{R}_d , respectively [34]. In our examples, the reference pressure is $P_{\text{ref}} = 0$ at all outlets. The vector of element unknowns for the Windkessel BC is

$$\mathbf{y}^{(e)} = \left[P_{\text{in}}^{(e)} \quad Q_{\text{in}}^{(e)} \right]^T. \quad (70)$$

The forward problem (19) is given by

$$\mathbf{E}^{(e)} = \left[-\mathcal{R}_d C \quad \mathcal{R}_p \mathcal{R}_d \right]^{(e)}, \quad (71)$$

$$\mathbf{F}^{(e)} = \left[-1 \quad \mathcal{R}_p + \mathcal{R}_d \right]^{(e)}, \quad (72)$$

$$\mathbf{c}^{(e)} = \left[P_{\text{ref}} \right]^{(e)}. \quad (73)$$

The derivatives of the nonlinear term \mathbf{c} vanish:

$$\left(\frac{\partial \mathbf{c}}{\partial \dot{\mathbf{y}}} \right)^{(e)} = \left(\frac{\partial \mathbf{c}}{\partial \mathbf{y}} \right)^{(e)} = \mathbf{0}. \quad (74)$$

C Sequential Monte Carlo algorithm

Figure 11 gives an overview of the iterative Sequential Monte Carlo (SMC) algorithm. Distributions in SMC are approximated by weighted particles according to

$$\pi_n(\boldsymbol{\theta}) \approx \sum_{i=1}^k w_n^{(i)} \delta_{\boldsymbol{\theta}_n^{(i)}}(\boldsymbol{\theta}), \quad (75)$$

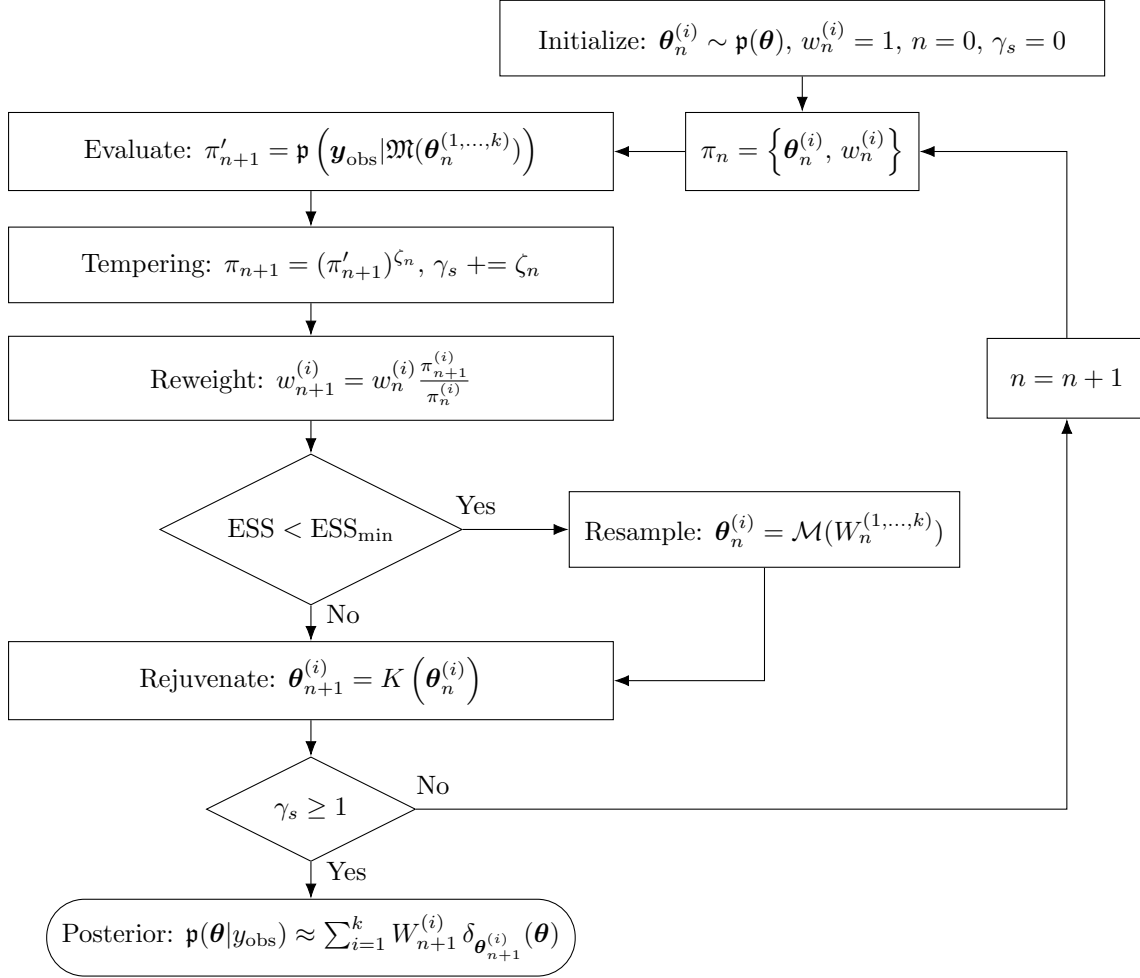


Figure 11: Sequential Monte Carlo algorithm.

wherein k denotes the number of particles and n is the iteration number. Each particle $\delta_{\theta_n^{(i)}}$ refers to a Dirac delta distribution at particle location θ_i . Distributions π_n are not necessarily normalized and, as such, should not be regarded as probability densities. A probability density is approximated with

$$\mathbf{p}_n(\boldsymbol{\theta}) \approx \sum_{i=1}^k W_n^{(i)} \delta_{\theta_n^{(i)}}(\boldsymbol{\theta}) \quad (76)$$

using the normalized weights

$$W_n^{(i)} = \frac{w_n^{(i)}}{\sum_{j=1}^k w_n^{(j)}}. \quad (77)$$

The algorithm is *initialized* by drawing k particles from the prior distribution with a uniform weight of one

$$\boldsymbol{\theta}_0^{(i)} \sim \mathbf{p}(\boldsymbol{\theta}), \quad w_0^{(i)} = 1, \quad \text{with } i \in \mathbb{N}_{>0}, i \leq k. \quad (78)$$

It is said that the particles *target* distribution π_0 (i.e., the prior). By evaluating the likelihood of each particle, the successor distribution can be derived

$$\pi_{n+1} = \mathbf{p}\left(y_{\text{obs}} | \mathfrak{M}(\boldsymbol{\theta}_n^{(1,\dots,k)})\right)^{\zeta_{n+1}}. \quad (79)$$

The particles are reweighted using importance sampling to target the new distribution π_{n+1}

$$w_{n+1}^{(i)} = w_n^{(i)} \cdot \frac{\pi_{n+1}^{(i)}}{\pi_n^{(i)}}. \quad (80)$$

The exponent ζ_n refers to the tempering step size and is part of the adaptive tempering reweighting strategy. It is selected based on the *effective sample size* ESS and the *resampling threshold* ESS_{\min} according to

$$\text{ESS}(w_{n+1}^{(1,\dots,k)}) \approx \zeta \text{ESS}_{\min} \quad (81)$$

with

$$\text{ESS} = \frac{1}{\sum_{i=1}^k (w^{(i)})^2}. \quad (82)$$

The effective sample size measures how well the weights are distributed between the particles and ensures an appropriate step size for each SMC step. With every iteration, the weights of some particles increase further, and others approach zero. Keeping many particles with (almost) no weights is inefficient, so the particles are *resampled*. Particles with high weights are duplicated, and particles with low weights are dropped. Herein, the systematic resampling strategy from Chopin et al. [32] is adopted. The particles are resampled based on a multinomial distribution $\mathcal{M}(W_n^{(1,\dots,k)})$ when the effective sampling size ESS is below the resampling threshold ESS_{\min} . The probability of a particle $\boldsymbol{\theta}^{(i)'}$ being resampled from particle $\boldsymbol{\theta}^{(i)}$ is determined by its relative weight

$$\mathbf{p}(\boldsymbol{\theta}^{(i)'}) = \frac{w^{(i)}}{\sum_{j=1}^k w^{(j)}} = W^{(i)}. \quad (83)$$

The resampling does not change the distribution targeted by the particles. To avoid a high correlation between particles after resampling (as some particles are duplicates of the same parameter vector), a rejuvenation step is added to move all particles according to

$$\boldsymbol{\theta}_{n+1}^{(i)} = K(\boldsymbol{\theta}_n^{(i)}), \quad (84)$$

using transition kernel K with stationary distribution π_{n+1} according to the proposal distribution in an MCMC step. The rejuvenation can be applied multiple times in a row. The process is terminated when the tempering exponent γ_s reaches ones, defined as

$$\gamma_s = \sum_{j=1}^{n+1} \zeta_j. \quad (85)$$

D Detailed zero-dimensional optimization results

The results of the optimization of 0D parameters from 0D ground truth and three-dimensional (3D) data are shown in Figures 12 and 13, respectively.

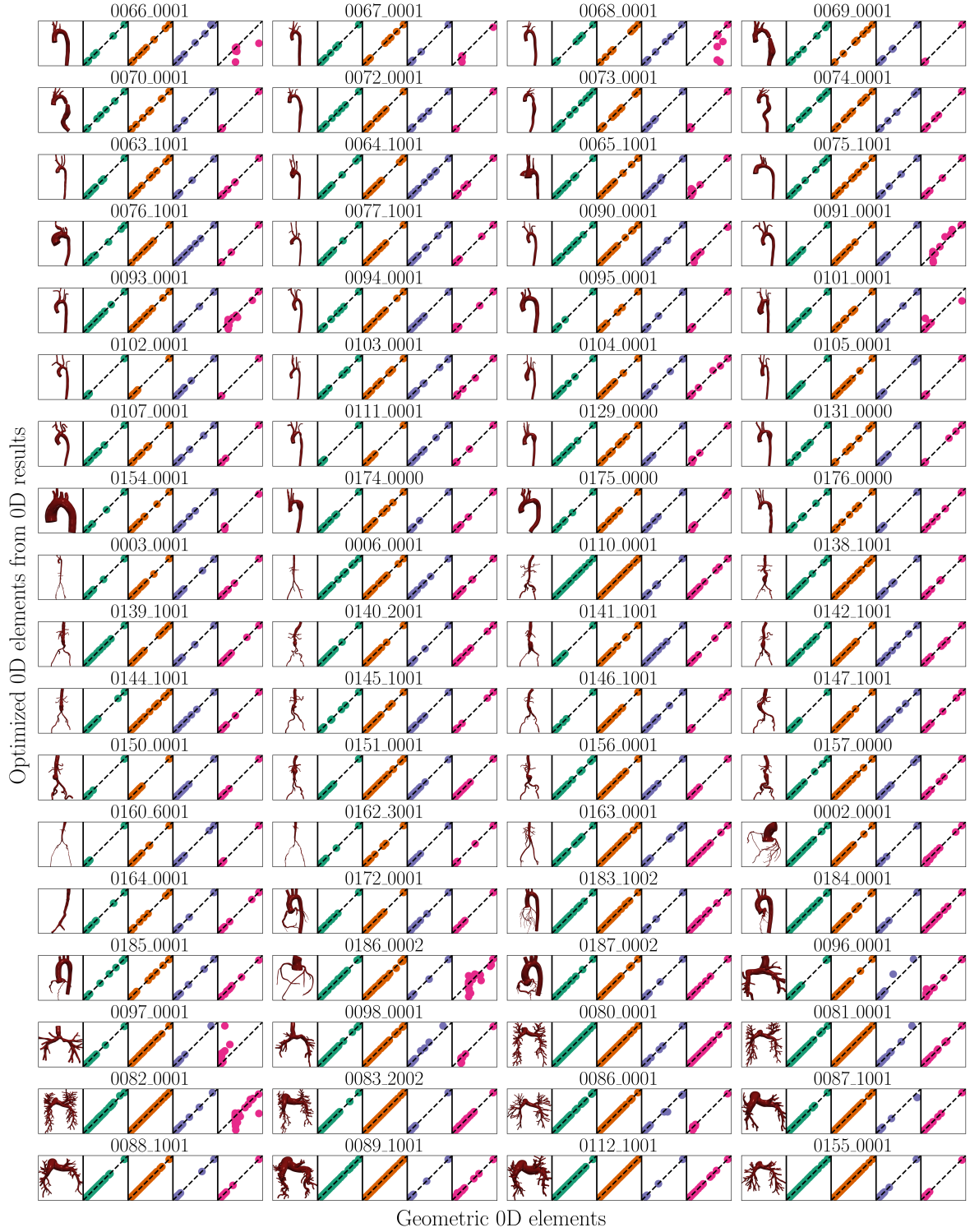


Figure 12: Correlation of optimized 0D elements from 0D ground truth data with 0D ground truth for all $N = 72$ models (aorta, aortafemoral, coronary, pulmonary). From left to right: \mathcal{R} (green), \mathcal{L} (orange), \mathcal{C} (purple), and \mathcal{S} (pink).

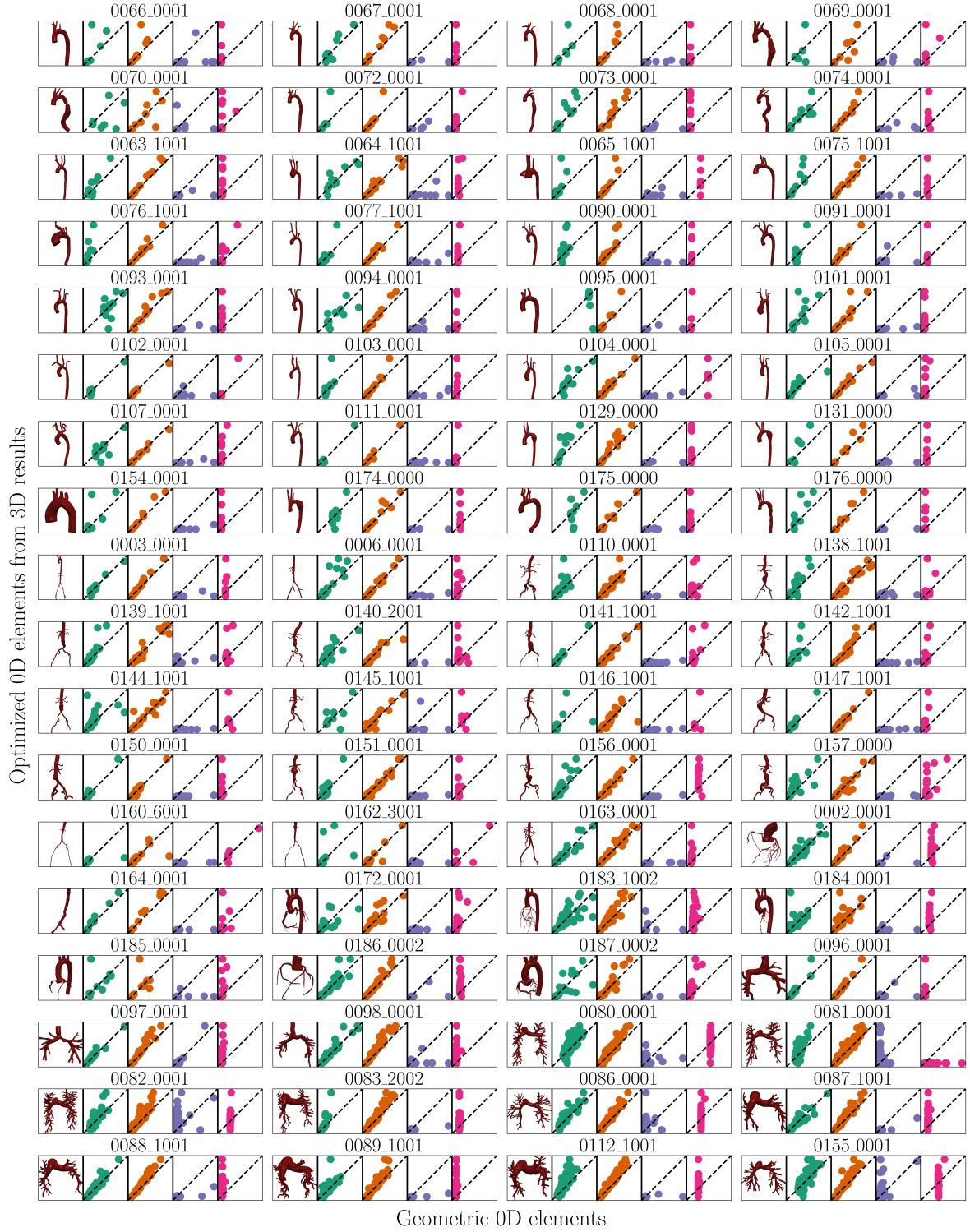


Figure 13: Correlation of optimized 0D elements from 3D data with 0D ground truth for all $N = 72$ models (aorta, aortafemoral, coronary, pulmonary). From left to right: \mathcal{R} (green), \mathcal{L} (orange), \mathcal{C} (purple), and \mathcal{S} (pink).

References

- [1] E. L. Schwarz, L. Pegolotti, M. R. Pfaller, and A. L. Marsden. Beyond cfd: Emerging methodologies for predictive simulation in cardiovascular health and disease. *Biophysics Reviews*, 4(1):011301, 2023.
- [2] I. E. Vignon-Clementel, C. Alberto Figueroa, K. E. Jansen, and C. A. Taylor. Outflow boundary conditions for three-dimensional finite element modeling of blood flow and pressure in arteries. *Computer Methods in Applied Mechanics and Engineering*, 195(29-32):3776–3796, 2006.
- [3] M. R. Pfaller, J. Pham, A. Verma, L. Pegolotti, N. M. Wilson, D. W. Parker, W. Yang, and A. L. Marsden. Automated generation of 0D and 1D reduced-order models of patient-specific blood flow. *International Journal for Numerical Methods in Biomedical Engineering*, 38(10), 2022.
- [4] P. J. Nair, M. R. Pfaller, S. A. Dual, D. B. McElhinney, D. B. Ennis, and A. L. Marsden. Non-invasive estimation of pressure drop across aortic coarctations: Validation of 0d and 3d computational models with in vivo measurements. *Annals of Biomedical Engineering*, 2024.
- [5] J. Schrauwen, J. Wentzel, A. van der Steen, and F. Gijzen. Geometry-based pressure drop prediction in mildly diseased human coronary arteries. *Journal of Biomechanics*, 47(8):1810–1815, 2014.
- [6] L. Garber, S. Khodaei, and Z. Keshavarz-Motamed. The critical role of lumped parameter models in patient-specific cardiovascular simulations. *Archives of Computational Methods in Engineering*, 29(5):2977–3000, 2021.
- [7] I. E. Vignon-Clementel, A. L. Marsden, and J. A. Feinstein. A primer on computational simulation in congenital heart disease for the clinician. *Progress in Pediatric Cardiology*, 30(1-2):3–13, 2010.
- [8] C. Chnafa, K. Valen-Sendstad, O. Brina, V. Pereira, and D. Steinman. Improved reduced-order modelling of cerebrovascular flow distribution by accounting for arterial bifurcation pressure drops. *Journal of Biomechanics*, 51:83–88, 2017.
- [9] M. Mirramezani and S. C. Shadden. A distributed lumped parameter model of blood flow. *Annals of Biomedical Engineering*, 48(12):2870–2886, 2020.
- [10] R. Pewowaruk, L. Lamers, and A. Roldán-Alzate. Accelerated estimation of pulmonary artery stenosis pressure gradients with distributed lumped parameter modeling vs. 3d CFD with instantaneous adaptive mesh refinement: Experimental validation in swine. *Annals of Biomedical Engineering*, 49(9):2365–2376, 2021.
- [11] I. S. Lan, W. Yang, J. A. Feinstein, J. Kreutzer, R. T. Collins, M. Ma, G. T. Adamson, and A. L. Marsden. Virtual transcatheter interventions for peripheral pulmonary artery stenosis in williams and alagille syndromes. *Journal of the American Heart Association*, 11(6), 2022.
- [12] J. D. Lee, J. Richter, M. R. Pfaller, J. M. Szafron, K. Menon, A. Zaroni, M. R. Ma, J. A. Feinstein, J. Kreutzer, A. L. Marsden, and D. E. Schiavazzi. A probabilistic neural twin for treatment planning in peripheral pulmonary artery stenosis. *arXiv*, 2023.
- [13] J. S. Tran, D. E. Schiavazzi, A. B. Ramachandra, A. M. Kahn, and A. L. Marsden. Automated tuning for parameter identification and uncertainty quantification in multi-scale coronary simulations. *Computers & Fluids*, 142:128–138, 2017.
- [14] A. L. Marsden. Optimization in cardiovascular modeling. *Annual Review of Fluid Mechanics*, 46(1):519–546, 2014.
- [15] G. Ninos, V. Bartzis, N. Merlemis, and I. Sarris. Uncertainty quantification implementations in human hemodynamic flows. *Computer Methods and Programs in Biomedicine*, 203:106021, 2021.
- [16] J. Nitzler, J. Biehler, N. Fehn, P.-S. Koutsourelakis, and W. A. Wall. A generalized probabilistic learning approach for multi-fidelity uncertainty quantification in complex physical simulations. *Computer Methods in Applied Mechanics and Engineering*, 400:115600, 2022.

- [17] J. Biehler, M. W. Gee, and W. A. Wall. Towards efficient uncertainty quantification in complex and large-scale biomechanical problems based on a bayesian multi-fidelity scheme. *Biomechanics and modeling in mechanobiology*, 14:489–513, 2015.
- [18] J. Biehler, M. Mäck, J. Nitzler, M. Hanss, P.-S. Koutsourelakis, and W. A. Wall. Multifidelity approaches for uncertainty quantification. *GAMM-Mitteilungen*, 42(2):e201900008, 2019.
- [19] P.-S. Koutsourelakis. Accurate uncertainty quantification using inaccurate computational models. *SIAM Journal on Scientific Computing*, 31(5):3274–3300, 2009.
- [20] D. Nolte and C. Bertoglio. Inverse problems in blood flow modeling: A review. *International Journal for Numerical Methods in Biomedical Engineering*, 38(8), 2022.
- [21] R. L. Spilker and C. A. Taylor. Tuning multidomain hemodynamic simulations to match physiological measurements. *Annals of Biomedical Engineering*, 38(8):2635–2648, 2010.
- [22] M. Ismail, W. A. Wall, and M. W. Gee. Adjoint-based inverse analysis of windkessel parameters for patient-specific vascular models. *Journal of Computational Physics*, 244:113–130, 2013.
- [23] K. Menon, J. Seo, R. Fukazawa, S. Ogawa, A. M. Kahn, J. C. Burns, and A. L. Marsden. Predictors of Myocardial Ischemia in Patients with Kawasaki Disease: Insights from Patient-Specific Simulations of Coronary Hemodynamics. *Journal of Cardiovascular Translational Research*, 16(5):1099–1109, 2023.
- [24] K. Menon, M. O. Khan, Z. A. Sexton, J. Richter, K. Nieman, and A. L. Marsden. Personalized coronary and myocardial blood flow models incorporating ct perfusion imaging and synthetic vascular trees. *medRxiv*, 2023.
- [25] S. Pant, B. Fabrèges, J. F. Gerbeau, and I. E. Vignon-Clementel. A methodological paradigm for patient-specific multi-scale CFD simulations: From clinical measurements to parameter estimates for individual analysis. *International Journal for Numerical Methods in Biomedical Engineering*, 30(12):1614–1648, 2014.
- [26] M. Spitieris, I. Steinsland, and E. Ingestrom. Bayesian calibration of Arterial Windkessel Model, 2022. arXiv:2201.06883 [stat].
- [27] J. Seo, C. Fleeter, A. M. Kahn, A. L. Marsden, and D. E. Schiavazzi. Multifidelity estimators for coronary circulation models under clinically informed data uncertainty. *International Journal for Uncertainty Quantification*, 10(5):449–466, 2020.
- [28] C. M. Fleeter, G. Geraci, D. E. Schiavazzi, A. M. Kahn, and A. L. Marsden. Multilevel and multifidelity uncertainty quantification for cardiovascular hemodynamics. *Computer Methods in Applied Mechanics and Engineering*, 365:113030, 2020.
- [29] D. P. Bertsekas and J. N. Tsitsiklis. *Introduction to probability*. Athena Scientific, 2002.
- [30] J. Kaipio and E. Somersalo. *Statistical and computational inverse problems*. Number v. 160 in Applied mathematical sciences. Springer, New York, 2005.
- [31] H. Gudbjartsson and S. Patz. The rician distribution of noisy mri data. *Magnetic Resonance in Medicine*, 34(6):910–914, 1995.
- [32] N. Chopin and O. Papaspiliopoulos. *An Introduction to Sequential Monte Carlo*. Springer, 2020.
- [33] N. Chopin. A sequential particle filter method for static models. *Biometrika*, 89(3):539–552, 2002. Publication Title: Biometrika Volume: 89 Issue: 3.
- [34] I. E. Vignon-Clementel, C. A. Figueroa, K. E. Jansen, and C. A. Taylor. Outflow boundary conditions for three-dimensional finite element modeling of blood flow and pressure in arteries. *Computer Methods in Applied Mechanics and Engineering*, 195(29-32):3776–3796, 2006.
- [35] I. Vignon-Clementel, C. Figueroa, K. Jansen, and C. Taylor. Outflow boundary conditions for 3d simulations of non-periodic blood flow and pressure fields in deformable arteries. *Computer Methods in Biomechanics and Biomedical Engineering*, 13(5):625–640, 2010.

- [36] M. E. Moghadam, I. E. Vignon-Clementel, R. Figliola, and A. L. Marsden. A modular numerical method for implicit 0d/3d coupling in cardiovascular finite element simulations. *Journal of Computational Physics*, 244:63–79, 2013.
- [37] M. R. Pfaller, J. Pham, N. M. Wilson, D. W. Parker, and A. L. Marsden. On the periodicity of cardiovascular fluid dynamics simulations. *Annals of Biomedical Engineering*, 49(12):3574–3592, 2021.
- [38] B. Steele, J. Wan, J. Ku, T. Hughes, and C. Taylor. In vivo validation of a one-dimensional finite-element method for predicting blood flow in cardiovascular bypass grafts. *IEEE Transactions on Biomedical Engineering*, 50(6):649–656, 2003.
- [39] J. P. Mynard and K. Valen-Sendstad. A unified method for estimating pressure losses at vascular junctions. *International Journal for Numerical Methods in Biomedical Engineering*, 31(7), 2015.
- [40] N. L. Rubio, L. Pegolotti, M. R. Pfaller, E. F. Darve, and A. L. Marsden. Hybrid physics-based and data-driven modeling of vascular bifurcation pressure differences. *arXiv*, 2024.
- [41] svSolver (<https://github.com/SimVascular/svSolver>), 2024.
- [42] M. Esmaily-Moghadam, Y. Bazilevs, and A. L. Marsden. A new preconditioning technique for implicitly coupled multidomain simulations with applications to hemodynamics. *Computational Mechanics*, 52(5):1141–1152, 2013.
- [43] svZeroDSolver (<https://github.com/SimVascular/svZeroDSolver>), 2024.
- [44] svSuperEstimator (<https://github.com/StanfordCBCL/svSuperEstimator>), 2024.
- [45] particles (<https://github.com/nchopin/particles>), 2023.
- [46] Vascular Model Repository (<https://vascularmodel.com>), 2024.
- [47] L. Pegolotti, M. R. Pfaller, N. L. Rubio, K. Ding, R. Brugarolas Brufau, E. Darve, and A. L. Marsden. Learning reduced-order models for cardiovascular simulations with graph neural networks. *Computers in Biology and Medicine*, 168:107676, 2024.
- [48] P. J. Nair, M. R. Pfaller, S. A. Dual, M. Loecher, D. B. McElhinney, D. B. Ennis, and A. L. Marsden. Hemodynamics in patients with aortic coarctation: A comparison of in vivo 4d-flow MRI and FSI simulation. In *Functional Imaging and Modeling of the Heart*, pages 515–523. Springer Nature Switzerland, 2023.
- [49] K. Bäumlér, V. Vedula, A. M. Sailer, J. Seo, P. Chiu, G. Mistelbauer, F. P. Chan, M. P. Fischbein, A. L. Marsden, and D. Fleischmann. Fluid–structure interaction simulations of patient-specific aortic dissection. *Biomechanics and Modeling in Mechanobiology*, 19(5):1607–1628, 2020.
- [50] A. Boccadifuoco, A. Mariotti, S. Celi, N. Martini, and M. Salvetti. Impact of uncertainties in outflow boundary conditions on the predictions of hemodynamic simulations of ascending thoracic aortic aneurysms. *Computers & Fluids*, 165:96–115, 2018.
- [51] M. N. Antonuccio, A. Mariotti, B. M. Fanni, K. Capellini, C. Capelli, E. Sauvage, and S. Celi. Effects of uncertainty of outlet boundary conditions in a patient-specific case of aortic coarctation. *Annals of Biomedical Engineering*, 49(12):3494–3507, 2021.
- [52] J. Chung and G. M. Hulbert. A time integration algorithm for structural dynamics with improved numerical dissipation: The generalized- α method. *Journal of Applied Mechanics*, 60(2):371–375, 1993.
- [53] K. E. Jansen, C. H. Whiting, and G. M. Hulbert. A generalized-alpha method for integrating the filtered navier–stokes equations with a stabilized finite element method. *Computer Methods in Applied Mechanics and Engineering*, 190(3-4):305–319, 2000.
- [54] K. Levenberg. A method for the solution of certain non-linear problems in least squares. *Quarterly of Applied Mathematics*, 2(2):164–168, 1944.
- [55] D. W. Marquardt. An algorithm for least-squares estimation of nonlinear parameters. *Journal of the Society for Industrial and Applied Mathematics*, 11(2):431–441, 1963.